# An evaluation of the Arabian Sea Mini Warm Pool's advancement during its mature phase using a coupled atmosphere-ocean numerical model

Sankar Prasad Lahiri[1], Kumar Ravi Prakash[1,2], Vimlesh Pant[1]

[1]Centre for Atmospheric Sciences, Indian Institute of Technology Delhi, India.

[2]Applied Physics Laboratory, University of Washington Seattle, WA, USA.

*Correspondence to*: Sankar Prasad Lahiri (sankarprasadlahiri2@gmail.com)

**Abstract.** A coupled atmosphere-ocean numerical model has been used to examine the relative contributions of atmospheric and oceanic processes in developing the Arabian Sea Mini Warm Pool (MWP). The model simulations were performed for three independent years, 2013, 2016, and 2018, through April-June, and the results were compared against observations. The model simulated sea surface temperature (SST) and sea surface salinity (SSS) bias were less than 1.75ºC and one psu, respectively; this bias was minimal in the MWP region. Moreover, the model simulated results effectively represented the presence of the MWP across the three different years. The mixed layer heat budget analysis indicated that the net surface heat flux raised the mixed layer temperature tendency of the MWP by a maximum of 0.1°C/day during its development phase. The vertical processes exerted a cooling impact on the temperature tendency throughout May and June with a maximum of -0.08ºC/day. Nonetheless, the decrease of net surface heat flux emerged as the dominant factor for the dissipation of the MWP. Further, four sensitivity numerical experiments were performed to investigate the comparative consequences of the ocean and atmosphere on the advancement of the MWP. The sensitivity experiments indicated that pre-April ocean conditions in years with a strong MWP resulted in a 136% increase in MWP intensity in years when MWP SST was close to climatology, which shows the primary role of oceanic preconditioning in determining MWP strength during strong MWP years. Once the oceanic preconditions are met, the atmospheric conditions of weak MWP years lead to an 82% reduction in MWP intensity relative to normal years, highlighting the detrimental impact of atmospheric forcing under such circumstances. Atmospheric conditions, particularly wind, are critical in influencing the spatial evolution and dissipation of MWP in the SEAS. A wind shadow zone, characterized by less potential turbulent kinetic energy that does not exist during weak MWP years, facilitates the spatial expansion of MWP in SEAS during moderate to strong MWP years.

## 1 Introduction

The North Indian Ocean's (NIO) associated ocean-atmosphere dynamics, including monsoon and cyclones, are well explored by researchers. One of the primary determinants in this interconnected process is the sea surface temperature (SST). During the pre-monsoon season, the southern region of the Arabian Sea experienced SST exceeding 28°C, which is associated with the larger Indo-Pacific Warm Pool. However, the highest temperature has been observed in the south-eastern Arabian Sea (SEAS) from late April to May, before the onset of the Indian Summer Monsoon. These patches of warm water in the SEAS are often referred to as the Arabian Sea Mini Warm Pool (MWP) (PV Joseph, 1990; Rao & Sivakumar, 1999; Seetaramayya & Master, 1984; Shenoi et al., 1999). The MWP SST remains 0.5ºC to 1ºC higher than the surroundings during this time. Because the MWP SST stays more than 30ºC, well above the minimal criteria for deep convection, it is thought to play a significant role in the Indian Summer Monsoon characteristics over Kerala (Deepa et al., 2007; Masson et al., 2005; Neema et al., 2012; R. R. Rao & Sivakumar, 1999).

Extensive studies have been conducted on the seasonal and interannual evolution of the MWP due to its noteworthy impact on regional climate dynamics (Akhil et al., 2023; Durand et al., 2004, 2007; Kurian & Vinayachandran, 2007; Mathew et al., 2018; Nyadjro et al., 2012; Rao & Sivakumar, 1999; Shenoi et al., 1999). According to Rao and Sivakumar (1999), the East India Coastal Current brings low salinity water to the SEAS in winter, which causes strong stratification and leads to the formation of the MWP in the following May. Shankar & Shetye (1997) explained the formation of the MWP in terms of the wave propagation phenomenon. The downwelling coastal kelvin wave travels along India's east coast after the summer monsoon has passed, eventually reaching the SEAS in November – December. Later, it is deflected westward by the Rossby Wave, forming the 'Laccadive High' (Bruce et al., 1994, 1998; Shankar & Shetye, 1997). The East India Coastal Current, triggered by the coastal kelvin wave on India's east coast, brings low salinity water to the SEAS and recirculates along the downwelling Laccadive High eddy in November and December. This low salinity water leads to the formation of a barrier layer in the SEAS (Gopalakrishna et al., 2005; Kumar et al., 2009; Masson et al., 2005; Murty et al., 2006; Shenoi et al., 1999). The barrier layer prevents the mixing of water above and below the thermocline (Lukas & Lindstrom, 1991) and traps the incoming shortwave radiation during the pre-monsoon season within the top few meters and thus increases the SST and leads to the MWP formation in next May (Hastenrath & Greischar, 1989). Masson et al. (2005) reported that the wintertime barrier layer intensifies the SST of the MWP by approximately 0.5°C.

Kumar et al. (2009) investigated the development of MWP using the Princeton Ocean Model. They stated that salinity has a significant impact on the formation of MWP. Using an ocean general circulation numerical model, Kurian & Vinayachandran (2007) discovered that the orographic influence of the western ghat acts as a wind barrier, increasing net surface heat flux and, hence, MWP intensity. According to Mathew et al. (2018), latent heat flux and incoming shortwave radiation, rather than wintertime freshening, influence the formation of MWP. Recently, Akhil et al. (2023) found that subsurface dynamics during the preceding winter have very little influence on the development of MWP.

Warm water can negatively affect the ocean ecosystem, particularly coral reefs (Abram et al., 2003; Doval & Hansell, 2000; Sarma, 2006). Given its proximity, any sudden increase in the intensity of the MWP could impact biological activity in the Laccadive High region. The MWP's impact also affects sound propagation dynamics (Kumar et al., 2007). Despite the evident importance, the formation mechanism of MWP remains a topic of ongoing scientific debate. The complex interplay of factors contributing to the genesis of the MWP, including winter salinity stratification and the presence of the Western Ghats, has been investigated in previous studies (Durand et al., 2004; Gopalakrishna et al., 2005; Kumar et al., 2009; Kurian & Vinayachandran, 2007; Masson et al., 2005; Nyadjro et al., 2012). However, recent findings by Akhil et al. (2023) suggested that the influence of winter salinity stratification on the MWP genesis might be less significant than previously thought. Moreover, a limited number of studies have focused on the air-sea interaction during the mature phase of the MWP, highlighting the need for further research in this area. Kumar et al. (2009) and Mathew et al. (2018) have explored these interactions, but comprehensive analyses remain sparse. Li et al. (2023) recently examined the Arabian Sea warm pool during its mature phase, emphasizing its seasonal and interannual variability using reanalysis datasets. While these studies contribute valuable insights, they primarily address variability over time rather than the specific processes driving the MWP's development and dissipation.

In this study, we examine the impact of the air-sea interaction on the progression of the Arabian Sea Mini Warm Pool using a coupled atmosphere-ocean numerical model. The coupled model employed in this study is calibrated for precise application on a seasonal time scale, which imposes limitations on the duration of simulations. Therefore, long-term simulations in each year are not feasible. Consequently, the present study focuses on configuring a regional coupled atmosphere-ocean numerical model to study the region-specific expansion and dissipation of the MWP. We also aim to elucidate the contribution of oceanic and atmospheric conditions to its growth over the years with distinct MWP intensity. The primary framework of the study is as follows: Section 2 provides an in-depth discussion of the data and methodology, including a detailed explanation of the coupled numerical model. Section 3 demonstrates the results along with the coupled model's ability to simulate temperature, salinity, and currents. Further, a few model sensitivity experiments have been incorporated to explore MWP characteristics and the influence of atmospheric and oceanic conditions across three different MWP events. Section 4 discusses the results and concludes the study with key findings.

## 2 Data & Methodology

### 2.1 Data

We utilized the Advanced Very High-Resolution Radiometer (AVHRR) SST dataset, part of the NOAA Climate Data Record program product suite. This dataset combines in-situ and satellite data from 1981 to the present using the optimal interpolation approach and is available on a daily time scale with a spatial resolution of 0.25° (Banzon et al., 2016). In this study, the coupled model's simulated SST is compared with the daily AVHRR SST data for the years 2013, 2016, and 2018. We used weekly SSS data from the European Space Agency's Sea Surface Salinity Climate Change Initiative (CCI) to validate the model's simulated sea surface salinity (SSS). This global Level 4 dataset is derived from a multi-sensor combination (SMOS, Aquarius, and SMAP). It spans from 2010 to 2020, offering a horizontal resolution of 50 km and a weekly temporal frequency (Boutin et al., 2021). The model's ability to reproduce ocean surface currents is confirmed using OSCAR surface current data with a horizontal resolution of 0.33° and a temporal resolution of 5 days (Bonjean & Lagerloef, 2002). The numerical model simulated vertical temperature and salinity is compared against AD10 buoy measurement data. AD10 is a moored buoy, and the National Institute of Ocean Technology (NIOT) is entrusted to deploy and collect the moored buoy data, later made available in the Indian National Centre for Ocean Information Services (INCOIS) data portal (https://incois.gov.in/portal/datainfo/mb.jsp). The vertical resolution of the buoy data varies with depth.

## 2.2 Model Details

The coupled atmosphere-ocean numerical model consists of the atmospheric model 'Advanced Research Weather Research and Forecasting' (WRF – ARW) and the ocean model 'Regional Ocean Modeling System' (ROMS). Both models are part of the Coupled Ocean-Atmosphere-Wave-Sediment Transport Modeling System (COAWST) (Warner et al., 2010). The model coupling toolkit (MCT) is used to couple the Atmospheric model WRF-ARW and ocean model ROMS (Jacob et al., 2005). Previously, this coupled numerical model was used to study the air-sea interaction during tropical cyclones (Chakraborty et al., 2022; Prakash et al., 2018; Prakash & Pant, 2017, 2020; Zambon et al., 2014), coastal processes (Carniel et al., 2016; Olabarrieta et al., 2011, 2012; Ricchi et al., 2016; Kumar & Nair, 2015) and monsoon deep depression over the Bay of Bengal (Chakraborty et al., 2023).

The ROMS model is a free-surface, hydrostatic, three-dimensional primitive equations (i.e., Reynolds averaged Navier-Stokes' equation) ocean model widely used in estuarine, coastal, and basin-scale research. The primitive equations in the ROMS model are solved using boundary-fit orthogonal, curvilinear coordinates on a staggered Arakawa C grid (Arakawa & Lamb, 1977). This model employs a terrain-following vertical sigma-coordinate system (Haidvogel et al., 2000; Phillips, 1957; Song & Haidvogel, 1994) and incorporates a variety of advection techniques, such as second and fourth-order center differences and third-order upstream biased method. Vertical mixing in ROMS is handled using either the local Generic Length Scale closure technique (Umlauf & Burchard, 2003) or the nonlocal k-profile boundary layer formulation (Large et al., 1994). Horizontal mixing of momentum and tracers can occur at vertical levels, geopotential, or isopycnal surfaces. Due to its very accurate and efficient physical and numerical algorithms, the ROMS model has been widely used to investigate the coastal, open ocean, and biogeochemical processes (Nigam et al., 2018; Paul et al., 2023; Sandeep et al., 2018; Seelanki et al., 2021).

The WRF - ARW atmospheric model is a non-hydrostatic, fully compressible model that predicts mesoscale processes using boundary layer physics schemes and various physical parameterizations (Skamarock & Klemp, 2008; Skamarock, 2008). On a horizontal Arakawa C grid and a vertical sigma-pressure coordinate, WRF - ARW estimates wind momentum components, surface pressure, longwave and shortwave radiative fluxes, dew point, precipitation, surface sensible and latent heat fluxes, relative humidity, and air temperature. WRF is intended to serve and support atmospheric research and operational forecasting needs (Dai et al., 2013). Parameterization schemes are available in microphysics, cumulus parameterization, planetary boundary layer, surface layer, land surface, and longwave and shortwave radiations, with multiple options for each process. In the COAWST modeling system, the WRF code has been modified to provide improved bottom roughness when computing bottom stress over the ocean (Warner et al., 2010). In addition to WRF and ROMS, the COAWST modelling framework also consists of wave and sediment transport models; however, these components are not used in this study.

### 2.3 Model Configuration and Experiment Design

The atmospheric component of the coupled numerical model (i.e., WRF model) supports a variety of parameterization schemes. In our WRF configuration we have incorporated the WRF Single-moment-6-class Scheme (Lim & Hong, 2010) as microphysics parameterization to represent grid-scale precipitation processes, the New Tiedtke Scheme for cumulus parameterization that illustrates sub-grid scale convection and cloud detrainment (Zhang & Wang, 2017), the Yonsei University Scheme (Hong et al., 2006) for planetary boundary layer physics, and the MM5 Similarity Scheme (Paulson, 1970). We have used the Unified Noah Land Surface Model (Tewari et al., 2004). At each time step, the atmospheric and land surface models calculate exchange coefficients and surface fluxes of the land or ocean layer and send them to the Yonsei University planetary boundary layer (Hong et al., 2006). The Dudhia Shortwave Scheme (Dudhia, 1989) is used for shortwave radiation parameterization, and the RRTM Scheme (Mlawer et al., 1997) is used for longwave radiation parameterization. The WRF domain has an outer domain resolution of 60 km (18°S to 38°N & 25°E to 95°E) and a nested domain with a 1:3 ratio (Fig. 1). It consists of 40 levels in the vertical direction. WRF is initialized with ERA5 data (Hersbach et al., 2020). The outer domain's lateral boundary condition is taken from ERA5 at 3-hour intervals.

The Ocean model ROMS employed in this study covers the Arabian Sea spanning 10°S - 30°N & 30°E - 85°E with a horizontal resolution of $\frac{1^o}{6}$. A terrain-following sigma coordinate system with 40 vertical levels was used, 20 concentrated in the upper 200 m. The ETOPO2 with 2-minute arc resolution data has been used to create the bathymetry data over the ROMS grid. The surface and bottom stretching parameters for sigma coordinates were set to $\theta_s$=7, & $\theta_b$=1.5, with a critical depth of 10m. The initial conditions and lateral boundary forcings for ROMS were derived from SODAv3.4.2 (Carton et al., 2018) data, having a horizontal resolution of $0.5° \times 0.5°$ with temporal availability of 5-day interval. Momentum and tracer particles were mixed horizontally along the geopotential surface. The non-local K-Profile Parameterization scheme (Large et al., 1994), which integrates the different unresolved processes associated with vertical mixing, was used to deal with vertical mixing. Horizontal and vertical advection of momentum were treated using third-order upstream and fourth-order centered advection schemes, respectively. The ROMS model employed 60-second baroclinic and 30-second barotropic time steps. Open boundary conditions for momentum and tracers on the southern and eastern boundaries used radiation schemes, allowing remote forcings from the Bay of Bengal and the southern Indian Ocean to influence the domain. Northern and western boundaries were closed in the ROMS model. Both the models were initialized from April and simulated till June. A 1-month spin-up period was sufficient to establish the mixed-layer dynamics (the MWP extends till the mixed layer depth (see Fig. S10 in the supplementary)).

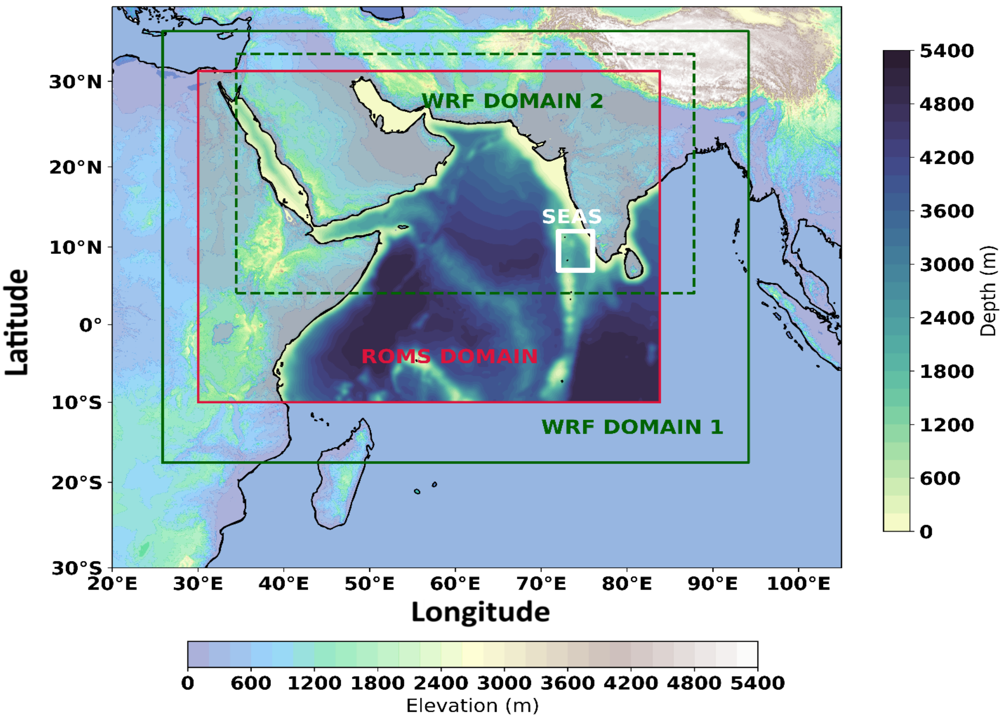

**Figure 1: WRF and ROMS model domains. The WRF domain is the green box, while the red box shows the ROMS model domain. Two domains of WRF are shown in solid and dashed green lines. The white box is the south-eastern Arabian Sea (core area of the MWP). Land elevation and ocean Depth are shown in two different contours.**

From the previous studies and our own experience (based on our several background experiments), we have observed that the coupled atmosphere-ocean numerical model (part of the COAWST model) would be more accurate when the simulation is up to the seasonal scale. Therefore, to assess the MWP using this coupled model, we ran the model for about 80 days for three independent years (2013, 2016, and 2018), which had distinct MWP characteristics (based on the interannual variation of the MWP area. See Fig. S1 in the supplementary). At every 15 minutes, the WRF and ROMS models interchange variables. While SST is the sole variable that is transferred from ROMS to WRF, other parameters, including 2m air temperature, mean sea level pressure, 10 meters u and v wind velocity, longwave and shortwave radiation, rainfall, and relative humidity, are exchanged from WRF to ROMS (readers are referred to Warner et al. 2010 for more details regarding the coupled model). Each run is initialized on seperately April 1 and run to June 20 each year, and the output is saved at a daily frequency. The first month of each simulation was used for spin-up and is not included in the analysis (except for the mixed layer heat budget analysis (Fig. 11)). We named this set of runs the control experiment (CNTRL), where we used the SODA and ERA5 data for actual oceanic and atmospheric conditions. Later, to investigate the factors contributing to the evolution of MWP, we designed and performed four idealized numerical experiments using the coupled atmosphere-ocean model with a one-way coupling mode. We modified the oceanic and atmospheric conditions in these experiments, as detailed in Table 1. In 2018, the MWP area was closer to climatology (Fig. S1 in supplementary). Hence, this year is used as the base year, and in all four sensitivity experiments, the forcings of the two other years are fed into the 2018 control run.

Table 1: List of model sensitivity experiments

| Experiments Name | Ocean model initial & boundary forcing year | Atmospheric forcing year |
|---|---|---|
| Control | 2018 | 2018 |
| $S_{ocean2013}$ | 2013 | 2018 |
| $S_{atmos2013}$ | 2018 | 2013 |
| $S_{ocean2016}$ | 2016 | 2018 |
| $S_{atmos2016}$ | 2018 | 2016 |

## 2.4 Mixed Layer Heat Budget

The mixed layer heat budget provides a detailed analysis of factors that can contribute to the change in the mixed layer temperature and is calculated using the formula outlined in (Akhil et al. 2023; Foltz & McPhaden 2009; Girishkumar et al. 2017; Nyadjro et al. 2012; Prakash & Pant 2017; Stevenson & Niiler 1983; Vialard et al. 2008) and given as:

$$\frac{\partial T}{\partial t} = \frac{Q_{net}}{\rho C_p h} - \left(u\frac{\partial T}{\partial x} + v\frac{\partial T}{\partial y}\right) + H\left[W_{-h} + \frac{\partial h}{\partial T}\right]\left[\frac{T_h - T}{h}\right] + Residuals \qquad (1)$$

Different terms in the above equation's right-hand side (RHS) contribute to temperature tendency differently; the first term on the RHS is the contribution from net surface heat flux; the second is from horizontal advection; and the third is from vertical process and entrainment. T is the average temperature of the mixed layer, t is the time (in days), and h is the mixed layer depth (MLD). Meridional and zonal velocity at MLD is given by u, and v. $Q_{net}$ is the net surface heat flux. Here, we have not considered the penetrative shortwave radiation below the MLD. H is the Heaviside step function and is expressed as $H = 0,\ if\left[W_{-h} + \frac{\partial h}{\partial T}\right] < 0$ or $H = 1,\ if\left[W_{-h} + \frac{\partial h}{\partial T}\right] > 1$. $W_{-h}$ is the vertical velocity. $T_h$ is the temperature just below (5 m) the depth of the MLD. The residual term represents contributions from other processes, such as diffusion. The units of all the terms here are in $^{o}$C.day$^{-1}$. In this study, the depth at which the subsurface temperature decreases by 1$^{o}$C as compared to the surface is used as the isothermal layer depth (ILD) (Kara et al., 2000; Shee et al., 2019; Sprintall & Tomczak, 1992). The MLD is calculated following Shee et al. (2019) as follows.

$$\sigma_{t(z=h)} = \sigma_{t(z=0)} + \Delta T \frac{d\sigma_t}{dt}$$

Where $\Delta T$ is the 1°C temperature criteria for ILD, and $\frac{d\sigma_t}{dt}$ is the coefficient of thermal expansion.

## 2.5 Potential Turbulent Kinetic Energy ($P_{TKE}$):

The production of turbulent kinetic energy ($P_{TKE}$) is used to understand the convective mixing caused by the relative contributions of wind stress (wind-forced momentum flux), freshwater flux (E - P) (haline buoyancy flux), and net surface heat flux (thermal buoyancy flux) (Shankar et al., 2016). $P_{TKE}$ is calculated using the expression given in Han et al. (2001) and Rao et al. (2002) and expressed as:

$$P_{TKE} = \rho u_*^3 + \left[-\frac{\alpha 0.5 gkMLDQ_{net}}{C_p} + 0.5\rho gkMLD\beta(E-P)S_0\right]$$

Where, $u_* = \sqrt{\frac{\tau}{\rho}}$ is the frictional velocity, $\tau$ is the wind stress, $\rho$ is the density of the seawater (1026 kg.m$^{-3}$), $k$ = 0.42 is the Von Kärmän constant, and g is the acceleration due to gravity. E is the evaporation rate, and P is the precipitation. $S_0$ is the salinity of the ML. $Q_{net}$ is the net surface heat flux. The thermal expansion coefficient ($\alpha$) and haline contraction coefficient ($\beta$) are taken as $\alpha$ = -0.00025 K$^{-1}$ and $\beta$ = 0.00785 psu$^{-1}$, respectively, following studies by Shankar et al. (2016) and He et al. (2020). $C_p$ (= 4187 J kg $^{-1}$) is the ocean's specific heat capacity. The first term on the right-hand side of the above equation represents $P_{TKE}$ due to wind stirring. The first term in the bracket is the $P_{TKE}$ due to thermal buoyancy representing the effect of net surface heat flux, and the second term is $P_{TKE}$ due to the haline buoyancy, which indicates the impact of freshwater change. The wind-stirring term, by definition, cannot be negative. A positive thermal buoyancy flux implies that heat is lost from the ocean, which causes MLD to deepen. On the other hand, the positive haline buoyancy flux causes more evaporation, which leads to an increase in MLD due to increased salinity (He et al., 2020; Shankar et al., 2016; Shee et al., 2019). Results

## 2.6 Model Validation:

Figures 2, 3, and 4 compare the coupled model's simulated SST, SSS, and current to observation data in 2018, 2013, and 2016. The mean results and bias are then shown for each of the three years, from May 1 to June 20. The simulated SST effectively captured the cold SST along the Somalia coast across all the examined years, firmly aligning with AVHRR SST data (Fig 2). The SST bias remained within 1.5-2°C in all three experiments except in the northern Arabian Sea and along the Somalia coast. In the north Arabian Sea, a cold SST bias and a warm SST bias near the Somalia coast of more than 1°C are observed. In the tropical western Indian Ocean, a cold SST bias was also witnessed in 2013. Despite this, the SST bias remained consistent across the study period, with a minimal bias in the SEAS region (black box in Fig. 2). The model simulated surface salinity revealed a pronounced high salinity tongue in the northern Arabian Sea, a feature similarly observed in the ESA salinity data (Fig. 3). The coupled model effectively reproduced the low salinity water in the SEAS, with the salinity bias primarily within 0.5 psu across the entire domain, except for a few isolated areas reaching one psu. The Indian Ocean is well-known for its seasonally reversing monsoon current. The West India Coastal Current (WICC) transports high salinity water from the northern to southern Arabian Sea in May and June and is the primary driver of inter-basin mass transport (Schott et al., 2009; Schott & McCreary, 2001; Shankar et al., 2002). The model simulated surface currents accurately captured the WICC between May and June for all three years (Fig. 4). Furthermore, the representation of the summer monsoon current in the simulation was commendable (not shown here).

The coupled model's temperature and salinity profiles were confirmed against buoy measurements at the AD10 location (10.25°N, 72.25°E) (Fig. S2). We utilized the model's nearest point to the AD 10 location to serve this purpose. Before validation, the model-simulated data is interpolated to the vertical resolution of the AD10 buoy data. The AD10 buoy data were available at an hourly time scale from 2012 to 2020 and at a 3-hour frequency in 2021. Except for 2016, the AD10 temperature contains data gaps (Fig. S3 to S5). In 2018, the model temperature had a cold bias below 50m deep at the buoy location. In 2013 and 2016, the model's simulated temperature had a positive bias of less than 1°C within the top 50 m. Although the vertical temperature is consistent with the AD10 buoy data, the model-simulated salinity data indicated more discrepancies in 2018. Aside from that, the model's represented salinity stayed within one psu bias in 2013 and 2016, with only a few areas exceeding this limit in 2013. The MWP does not extend beyond the mixed layer depth (Akhil et al., 2023 and Fig. S10 in supplementary), and our model-estimated temperature and salinity remain in excellent accord within this depth. To further examine the vertical temperature performance of the model, we conducted a detailed temporal correlation analysis of the simulated temperatures for three distinct control experiments, corresponding to the years 2018, 2013, and 2016. This analysis is performed against observational data obtained from the AD10 buoy location, with calculations made at various depths, specifically at 1, 5, 10, 15, 20, 30, 50, and 100 meters. The results of this statistical assessment are graphically represented in a Taylor diagram (Fig. 5). The points at 50 m depth are out of the range of axes for 2013. Across all three control experiments, the standard deviation of the simulated temperature values generally ranged between 0.3 and 1.5, with a few exceptions at certain depths. Additionally, the correlation coefficient between the model simulations and the buoy observations varied from 0.5 to 0.98, indicating a moderate to strong agreement depending on the depth considered.

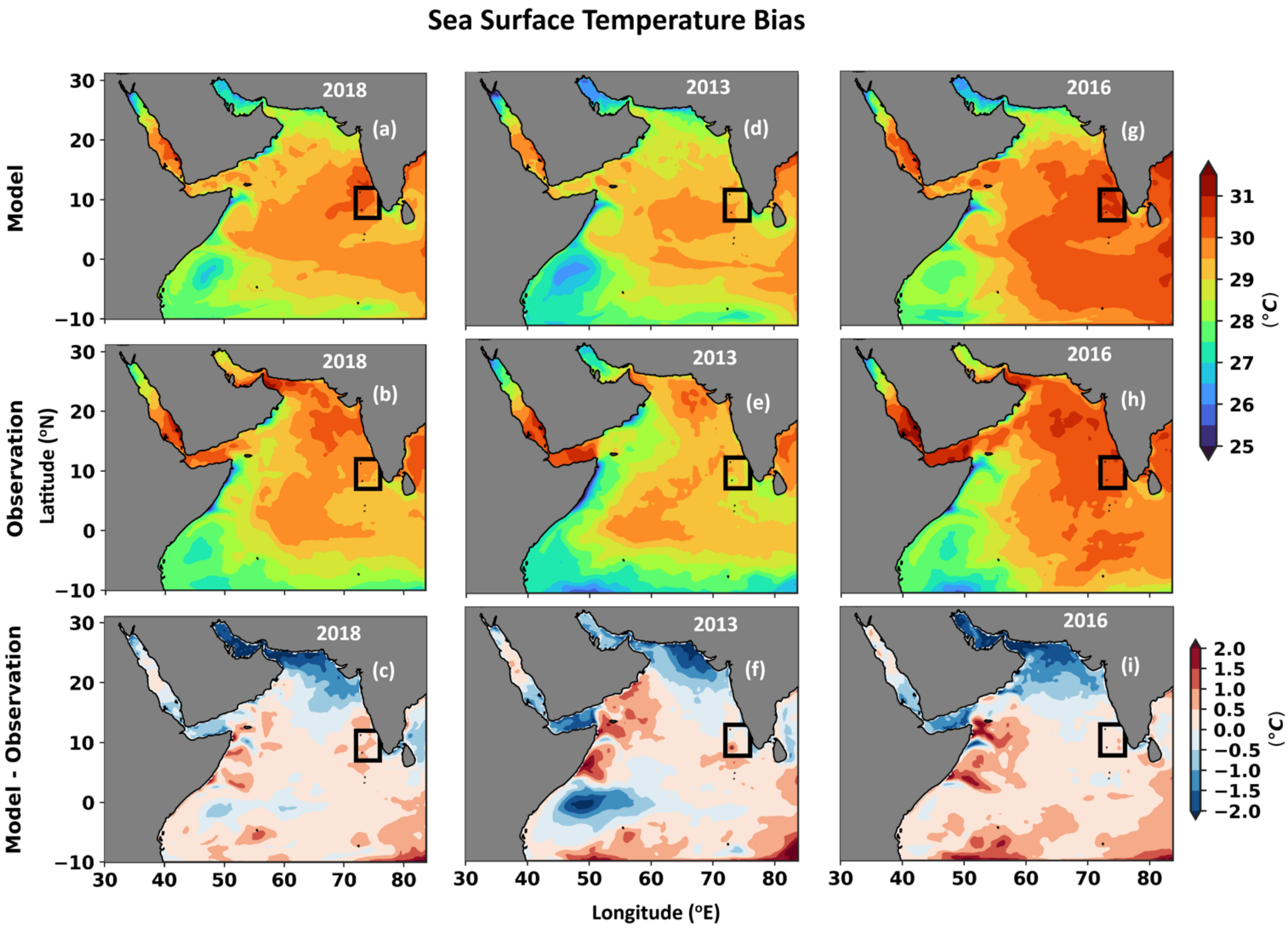

**Figure 2: Comparison of model-simulated sea surface temperature (SST) and NOAA-AVHRR surface temperature. Panels (a), (d), and (g) depict model-simulated SST for the years 2018, 2013, and 2016, respectively. Panels (b), (e), and (h) display NOAA-AVHRR SST for the corresponding years. Panels (c), (f), and (i) illustrate the SST difference between model output and observation. The black box delineates the domain of interest, i.e., the MWP core region. The mean results and bias are shown for each of the three years, averaged from May 1 to June 20.**

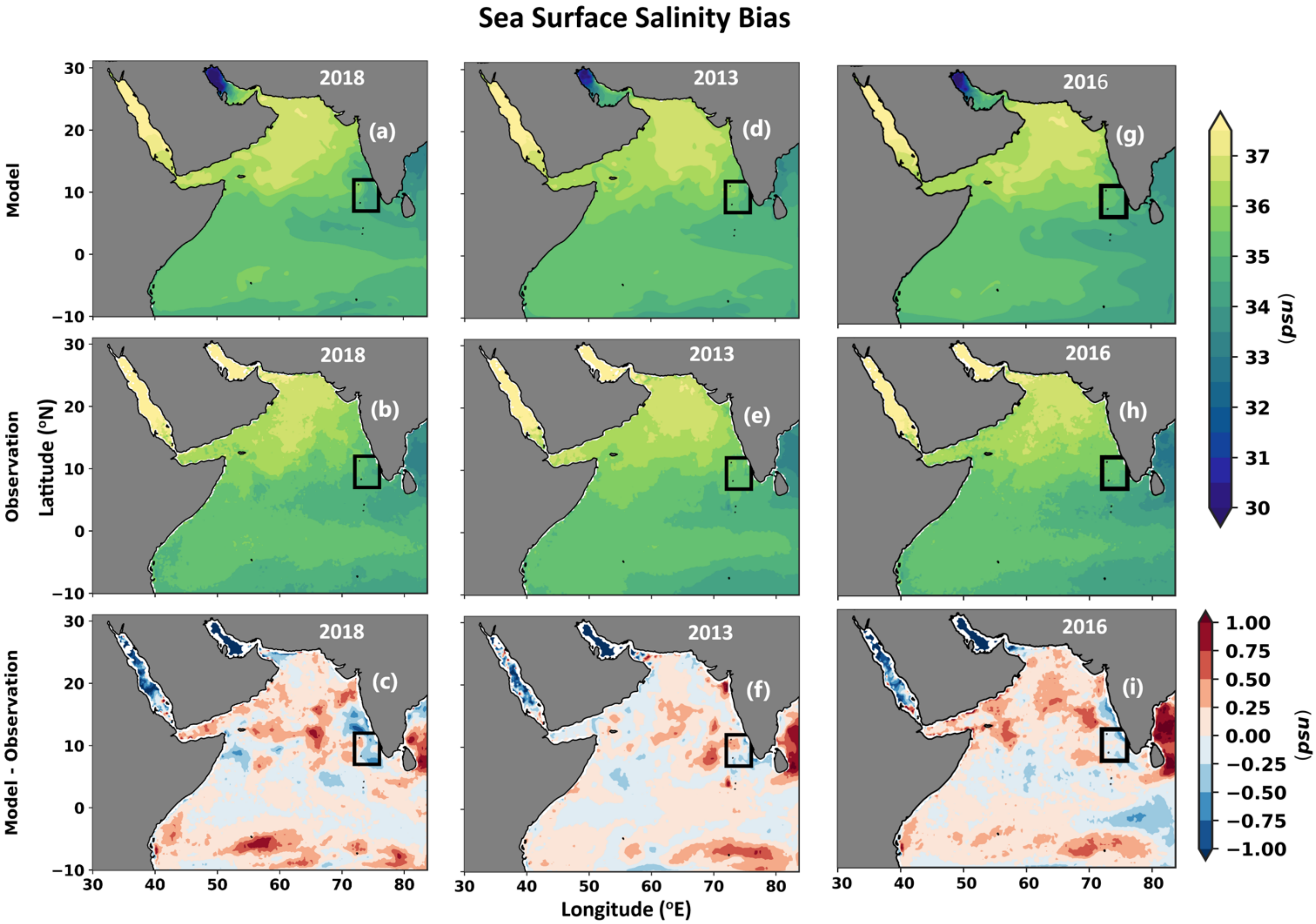

**Figure 3: Comparison of model-simulated sea surface salinity (SSS) and ESA-observed SSS. Panels (a), (d), and (g) depict model-simulated SSS for the years 2018, 2013, and 2016, respectively. Panels (b), (e), and (h) display observed SSS for the corresponding years. Panels (c), (f), and (i) illustrate the SSS difference between the model output and observation. The black box delineates the domain of interest, i.e., the MWP core region. The mean results and bias are shown for each of the three years, averaged from May 1 to June 20.**

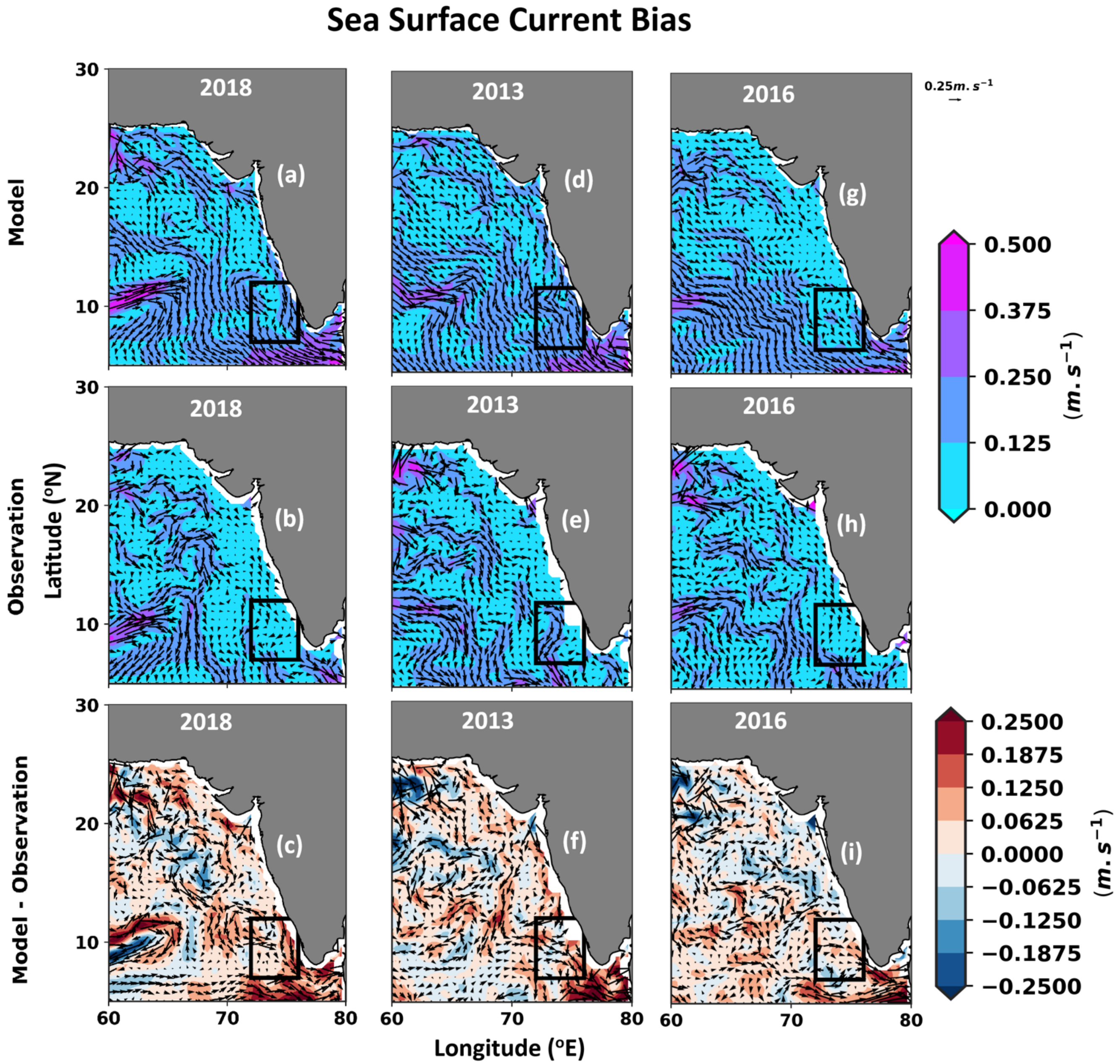

**Figure 4: Comparisons of model simulated currents against Oscar surface current. The first column from the left (a-c) is for 2018, the second is for 2013 (d-f), and the last is for 2016 (g to i). As the MWP forms near the western coast of India, the current patterns are shown in the adjacent region, not the whole model domain. Panels (c), (f), and (i) illustrate the difference between the resultant current and the direction between model output and observation. The black box delineates the domain of interest, i.e., the MWP core region. The mean results and bias are shown for each of the three years, averaged from May 1 to June 20.**

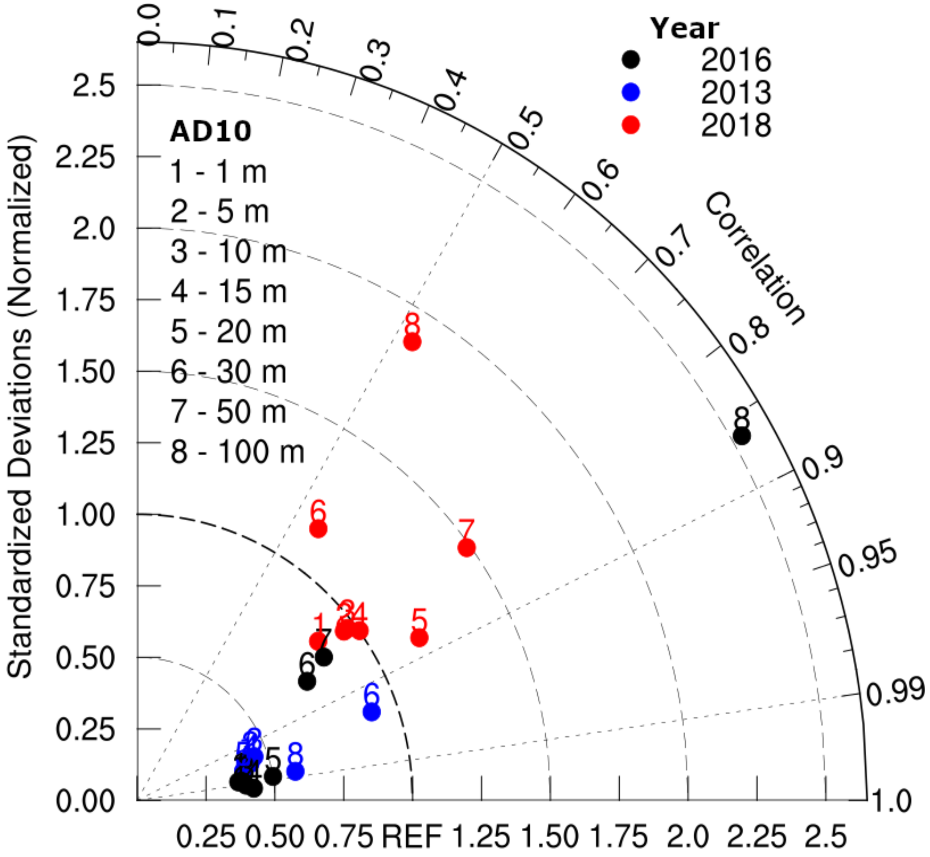

**Figure 5: Taylor diagram showing the temporal correlation and standard deviations of the model simulated temperature profile from the three years of model experiments with respect to measurements at the buoy AD10.**

### 2.7 Ocean surface characteristics during various phases of Arabian Sea Mini Warm Pool

Figure 6 shows the model simulated SST, wind stress, and salinity during the mature and dissipation days of MWP. The mature day of the MWP is characterized by the day when SST within the MWP core (shown by the white box in Fig. 1) reaches its highest magnitude in May. The dissipation day is determined when the MWP SST equalizes that of the surrounding water following its mature phase. In addition, the days from the mature to the dissipation are termed the dissipation phase. Previous studies (Li et al., 2023; Rao & Sivakumar, 1999; etc.) have used 30ºC to identify the MWP. A consistent bias of 0.5ºC is noticed in SEAS; hence, our study used a threshold of 30.5°C to detect the MWP. In 2018, the SST within the MWP core reached above 31°C on May 20, after which it gradually decreased (Fig. 6a-c). During the mature day in 2018, wind stress over the SEAS was low compared to its surroundings, but wind speed increased considerably afterward. Subsequently, the MWP SST matched the temperature of the surrounding sea by June 8. Despite the absence of the MWP in 2013, the same MWP mature and dissipation day as in 2018 was used for demonstrative purposes (as shown in Fig. 6d-f). In 2016, the MWP matured on May 4 with a larger spatial area than the previous two years (Figs. 6g-i). During the mature day, the wind stress was minimal in the southern Arabian Sea (Fig. 6g). Once the wind stress escalated, the MWP entirely dissipated by June 6, 2016 (Fig. 6h and i).

Table 2: Details of mature and dissipation days in each year with the threshold used to identify the MWP

| Year | Mature Day | Dissipation Day | Threshold |
|---|---|---|---|
| 2018 | May 20 | June 8 | 30.5°C |
| 2013 | May 20 | June 8 | 30.5°C |
| 2016 | May 4 | June 6 | 30.5°C |

Salinity in the vicinity of the MWP was lower during its mature day (<34 psu except in 2013) but increased during its dissipation day (>35.2 psu) (Fig. 7a to 7i). In the MWP core region, salinity was notably less in 2018 compared to the other two years (Fig. 7a). In 2016, while the MWP was in its mature stage, low salinity water (less than 34 psu) was detected south of SEAS, slightly outside the core MWP area (Fig. 7g). The salinity was more in the SEAS during the mature day in 2013 as compared to 2016 and 2018.

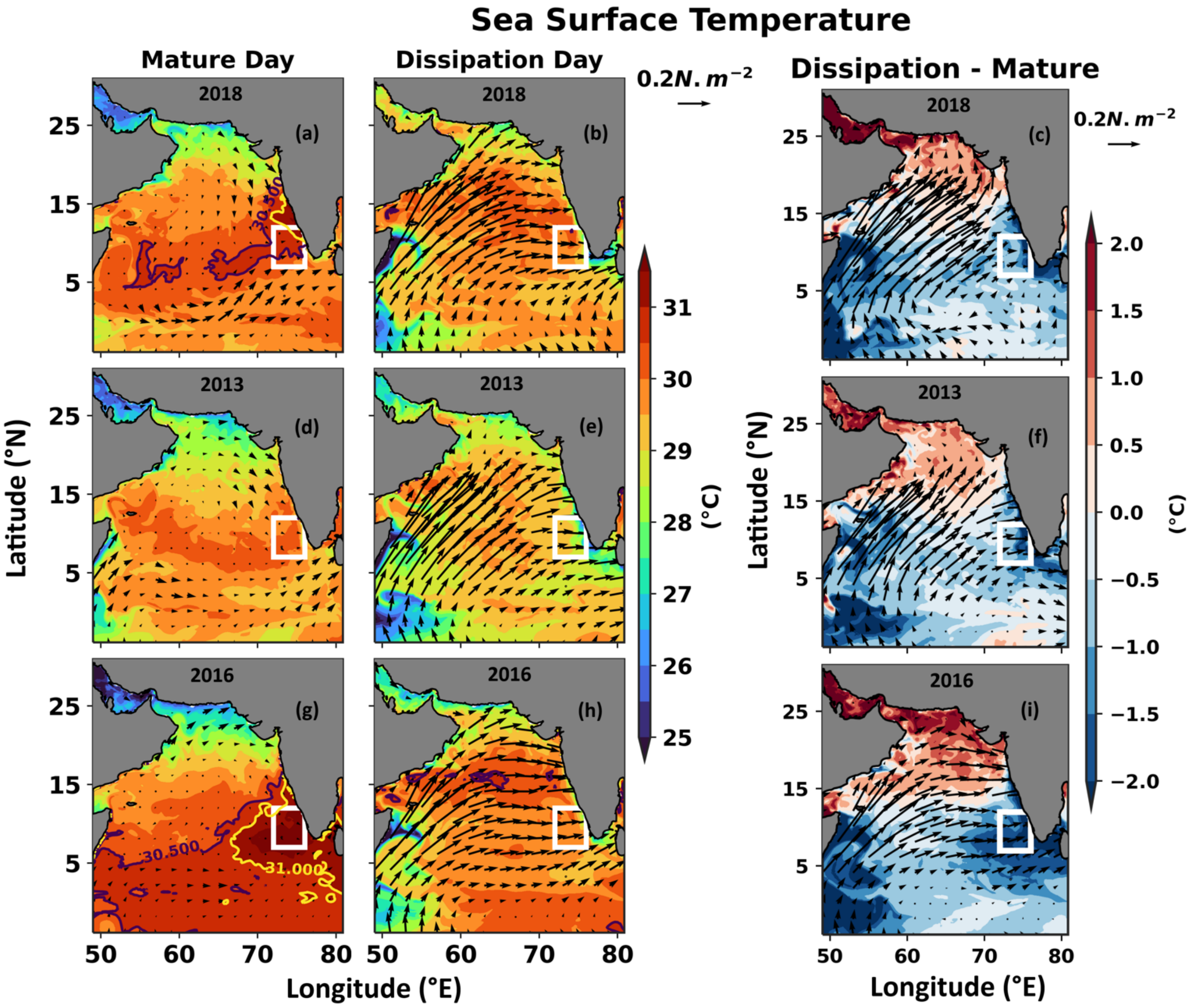

**Figure 6: Comparison of SST overlaid by wind stress on mature and dissipation days in 2018 (a-c) (MWP strength close to climatology), 2013 (d-f) (MWP was absent), and 2016 (g-i) (MWP was intense). (c), (f), and (i) show the distinction between dissipation and mature day. The MWP's mature days are May 20, 2018, 2013, and May 4, 2016. The MWP's dissipation days were June 8, 2018, 2013, and June 6, 2016. The black and yellow contours represent 30.5°C and 31°C, respectively. The white box is the core MWP region.**

On the mature day of the MWP, there was a positive net surface heat flux across the Arabian Sea except for its southern flank (Fig. 8a, 8d, and 8g). However, as wind stress intensified during the dissipation phase, the net surface heat flux in the Arabian Sea transitioned to negative values in all the years (Fig. 8c, 8f, and 8i). Subsequently, four elements of the net surface heat flux are examined to understand its impact on the regional growth of the MWP in SEAS (Fig. S6 to S9 in supplementary).

The shortwave radiation flux was positive and contributed majorly to the net surface heat flux. Because of the clear sky, the shortwave radiation was higher in April – May (Li et al., 2023). However, once the southwesterly wind strengthened, the subsequent cloudiness blocked the incoming shortwave radiation flux. Consequently, the shortwave radiation flux in the SEAS reduced on dissipation day (Fig. S6c, S6f, and S6i in supplementary). The exchange of energy between the atmosphere and ocean is facilitated by turbulent processes, such as sensible and latent heat flux (Large & Pond, 1981). As the wind speed increased, the loss of the latent heat flux increased from the mature to the dissipation day in all the years (Fig. S8c, S8f, and S8i in supplementary).

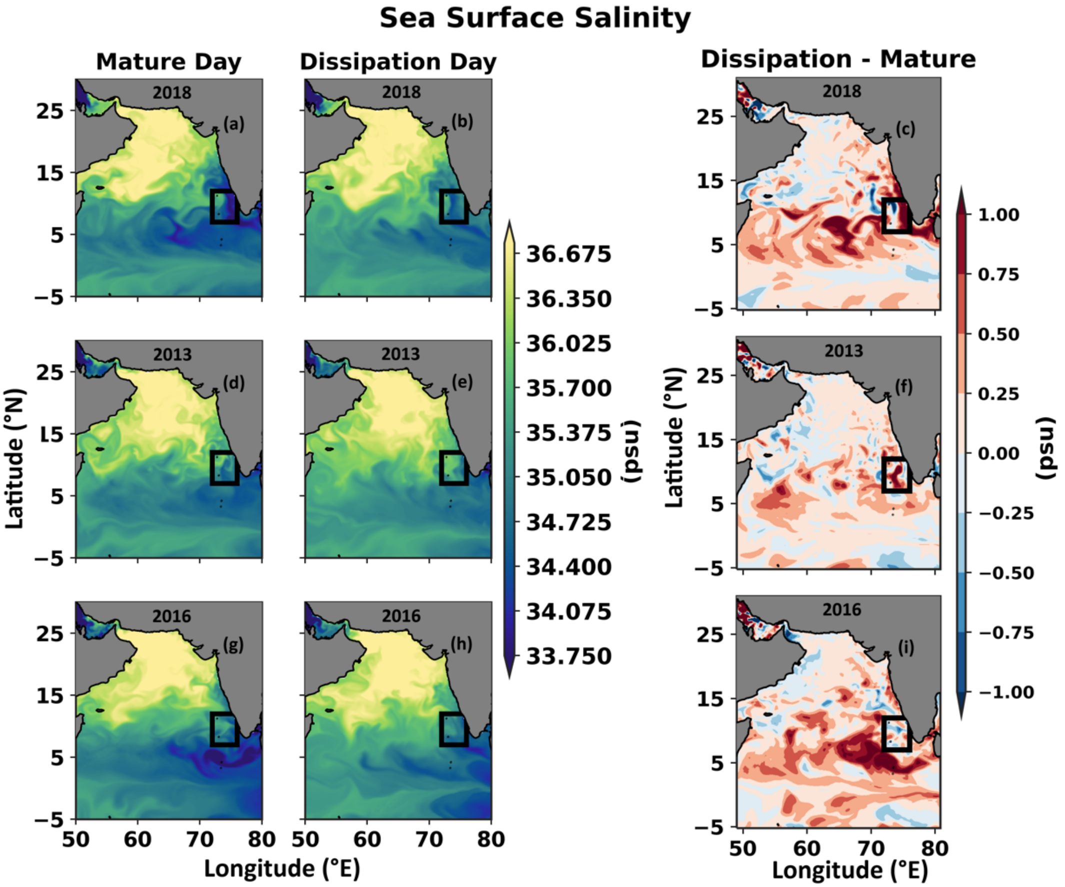

**Figure 7: Comparison of sea surface salinity on mature and dissipation days in 2018 (a-c) (MWP strength close to climatology), 2013 (d-f) (MWP was absent), and 2016 (g-i) (MWP was intense). (c), (f), and (i) show the distinction between dissipation and mature day. The MWP's mature days are May 20, 2018, 2013, and May 4, 2016. The MWP's dissipation days were June 8, 2018, 2013, and June 6, 2016. The black box is the core MWP region.**

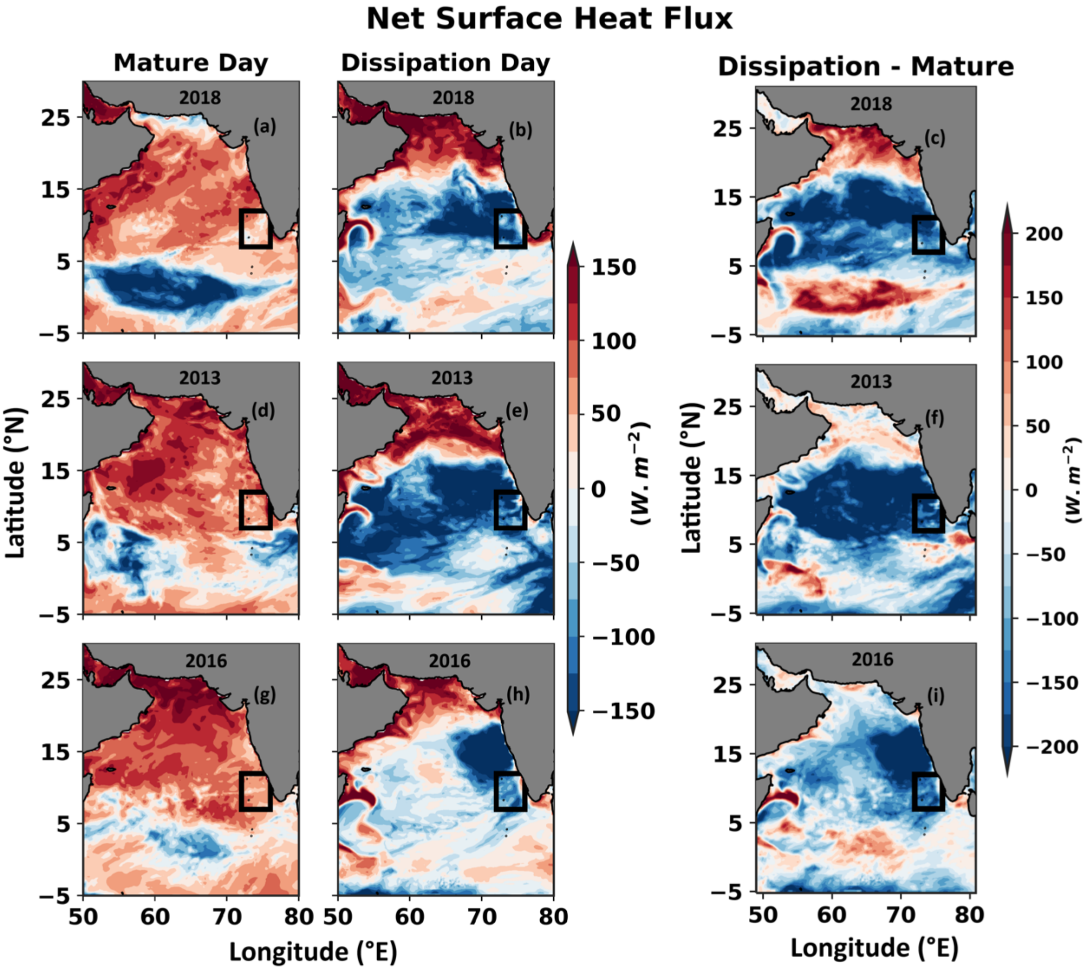

**Figure 8: Same as Fig. 7 but for net surface heat flux.**

## 2.8 Causative Factors

### *2.8.1* The Role of the Atmosphere and Ocean in the Formation of MWP

325 This section examines the relative contributions of the ocean and atmosphere to the development of the MWP through four sensitivity experiments (see Table 1 for details). In the $S_{ocean2013}$ and $S_{ocean2016}$ experiments, the ocean initial and boundary conditions from 2013 and 2016 replace those in the 2018 control experiment, respectively. The MWP remains very strong (weak) in the $S_{ocean2016}$ ($S_{ocean2013}$) experiment and reaches its maximum extent on May 20 (Fig. 9a and b is compared with 9c). An intense MWP was developed in the 2016 control experiment, and a similar MWP is also seen in $S_{ocean2016}$. The initial mean 330 pre-April ocean temperature in SEAS (initial condition temperature is averaged within the white box in Fig. 9 and 10 and to the MLD) was 0.35°C higher in 2016 (0.15°C lower in 2013) compared to 2018. Following the initial conditions, the MWP core temperature within the MLD was 0.6°C higher in $S_{ocean2016}$ (0.3°C lower in $S_{ocean2013}$) compared to the 2018 control

simulation during the mature day (Fig. S10d and S10e are compared with Fig. S10a in the supplementary). These results indicate that the pre-April ocean conditions strongly influence the intensity of the MWP.

Later, in the $S_{atmos2013}$ experiment, the 2013 atmospheric conditions were replaced with the 2018 control experiment's atmospheric conditions. MWP is absent in the 2013 control and $S_{atmos2013}$ experiments (Fig. 10a and 6d). Similarly, the 2016 atmospheric conditions replace those used in the 2018 control experiment, which is termed the $S_{atmos2016}$ experiment. A strong MWP was observed in the $S_{atmos2016}$ experiment (Fig. 10b), albeit with a lower intensity than in the 2016 control (Fig. 6g) and $S_{ocean2016}$ (Fig. 9b) experiment, indicating that pre-April ocean conditions were responsible for the formation of an intense MWP in the 2016 control experiment. In the $S_{atmos2016}$ and 2016 control experiments, the MWP matured on May 4. Similarly, the $S_{ocean2016}$ and 2018 control experiments have analogous atmospheric conditions, and the MWP matures on May 20 (Fig. 9b and 9c). These findings suggest that the atmospheric variables determine the spatial variability of the MWP as well as the day of maturation.

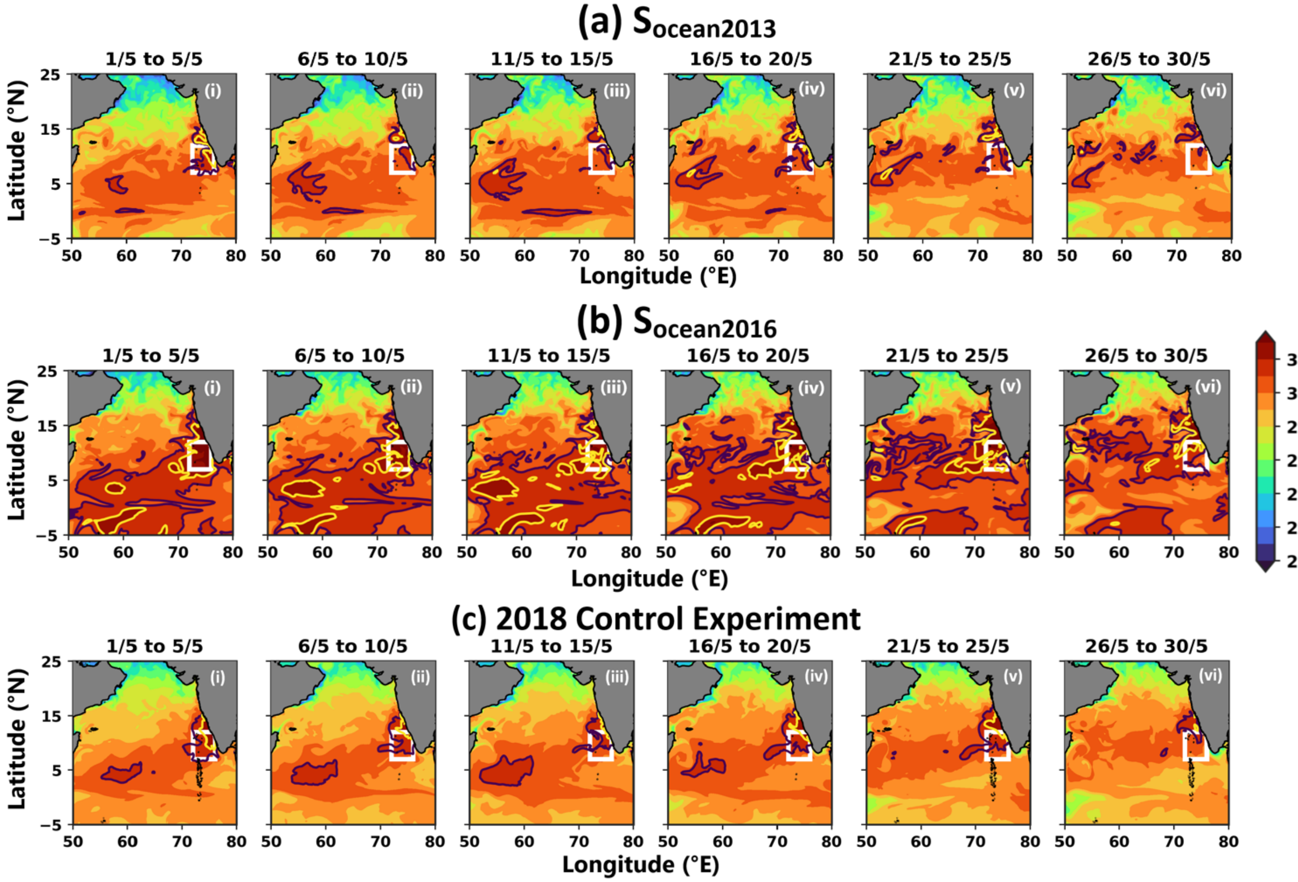

**Figure 9: 5-day average evolution of SST from May 1 to May 30 for the experiment (a) $S_{ocean2013}$, (b) $S_{ocean2016}$, and (c) 2018 control experiment. In these two experiments, the ocean's initial condition was replaced in 2013 and 2016 in the 2018 control experiment. See Table 1 for further details about the experiments. The black and yellow contours**

**represent 30.5°C and 31°C, respectively. The days associated with mean evolution are displayed at the top of each subplot. The white box is the core MWP region.**

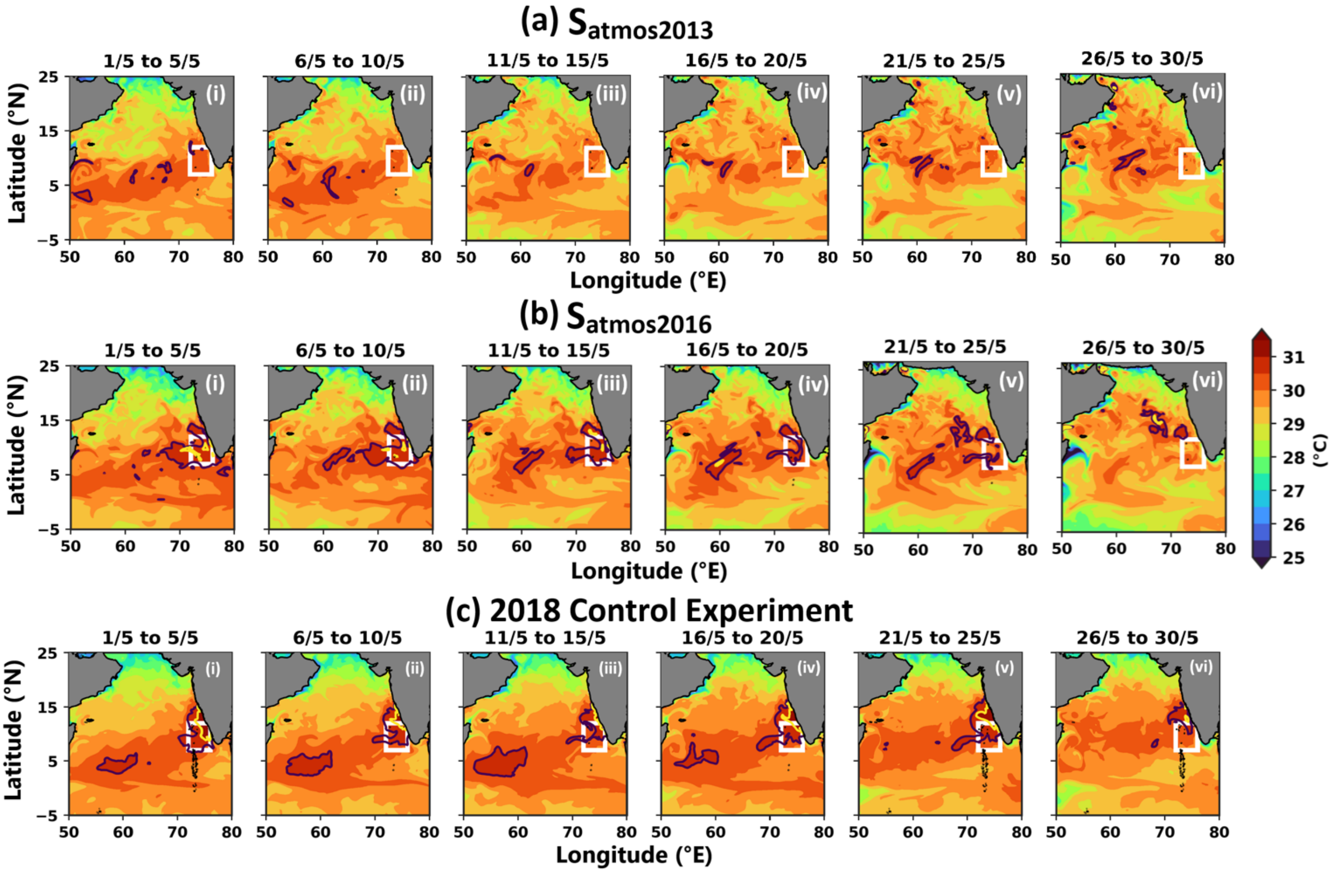

**Figure 10: 5-day average evolution of SST from May 1 to May 30 for the experiment (a) $S_{ocean2013}$, (b) $S_{ocean2016}$, and (c) 2018 control experiment. In these two experiments, the atmospheric condition was replaced in 2013 and 2016 in the 2018 control experiment. See Table 1 for further details about the experiments. The black and yellow contours represent 30.5°C and 31°C, respectively. The days associated with mean evolution are displayed at the top of each subplot. The white box is the core MWP region.**

The mixed layer heat budget in the core region of the MWP (72-76°E and 7-13°N) is analyzed to allow a better understanding of the factors contributing to its expansion and dissipation. The atmospheric conditions remain unchanged in the $S_{ocean2013}$, $S_{ocean2016}$, and 2018 control experiments. A dip in the net surface heat flux from 0.1°C.day$^{-1}$ to -0.07°C.day$^{-1}$ is noticed on May 8 in these three experiments. Later, this net surface heat flux supplied to the mixed layer temperature tendency with a maximum of 0.1°C per day from May 15 to May 18 (Fig. 11a, 11d, and 11e), and the MWP matured on May 20 thereafter. During the dissipation phase of the MWP, the net surface heat flux had an adverse impact on the temperature tendency in $S_{ocean2013}$, $S_{ocean2016}$, and 2018 control experiments. The vertical processes also had a cooling effect on the temperature tendency, which peaked at -0.09°C.day$^{-1}$ on May 26 in $S_{ocean2013}$, $S_{ocean2016}$, and 2018 control experiments. Even if the MWP was not apparent in the 2013 and $S_{atmos2013}$ experiments (both of these experiments have similar atmospheric conditions), the net surface heat flux caused a gain of 0.05°C temperature within the mixed layer on May 20 (Fig. 11b and 11f). Once the MWP reached its mature day, the vertical processes and the net surface heat flux had a detrimental effect on the temperature tendency in the $S_{atmos2016}$ and 2016 control experiments (Fig. 11c and 11g). In all control and sensitivity experiments, the temperature tendency is negatively impacted by the vertical processes during May and June; nevertheless, the net surface heat flux is the primary driver behind the variation of the temperature tendency from the mature to the dissipation day. The horizontal advection had a very minimal influence on the temperature tendency. Thus, atmospheric conditions modulate the mature and dissipation of the MWP.

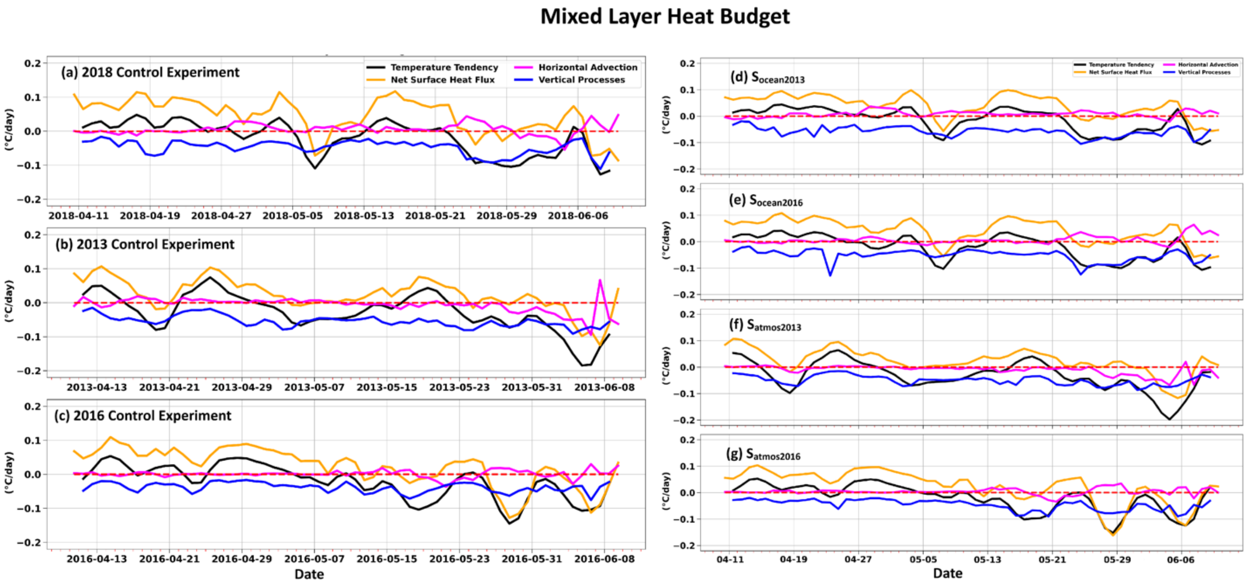

**Figure 11: Area averaged (72- 76°E and 7-13°N, i.e., the white box shown in Fig. 1) mixed layer heat budget for three control ((a) 2018 control experiment, (b) 2013 control experiment, and (c) 2016 control experiment) and four sensitivity experiments ((d) $S_{ocean2013}$, (e) $S_{ocean2016}$, (f)$S_{atmos2013}$, and (g) $S_{atmos2016}$). In the sensitivity experiments, the oceanic and atmospheric conditions have been changed to various years; thus, only the day and month are kept on the x-axis (d to g). For better understanding, the mixed layer heat budget is shown from April 10th, even though we have considered April 1st to April 30th as the spin-up time.**

To better assess the atmosphere's and ocean's relative contribution to the MWP intensity across different experiments, we introduced the MWP intensity index. This index is defined as:

$$MWP\ intensity\ index\ =\ MWP\ area\ on\ mature\ day\ X\ \Delta T_{avg}$$

Where $\Delta T_{avg}$ represented the average temperature change within the MWP area from its initial condition to the mature day.

In the 2016 control experiment, the MWP intensity index reached its highest value, corresponding to the warmest MWP SST and the most extensive area (Fig. 12). In contrast, the MWP was weak in the 2013 control experiment, and so as the MWP intensity index. In the $S_{ocean2013}$ experiment, where the ocean's initial and boundary conditions were modified from 2018 to 2013, the MWP Intensity Index decreased by 8.5% compared to the 2018 control experiment. However, a substantial reduction of 82% in the MWP intensity index was found when the atmospheric forcings were altered to 2013 in the $S_{atmos2013}$ experiment, highlighting the adverse effect of the atmospheric environment on the formation of MWP.

Conversely, the $S_{ocean2016}$ experiment, which replaced the 2018 oceanic initial and boundary condition with that of 2016, showed a 136% rise in the MWP intensity index compared to the 2018 control experiment. However, when the atmospheric condition was adjusted to 2016 in the $S_{atmos2016}$ experiment, the MWP intensity index decreased by 41%, indicating that the ocean precondition was the primary factor in the genesis of the intense MWP in 2016 and that the atmospheric condition later favored its development (Fig. 12).

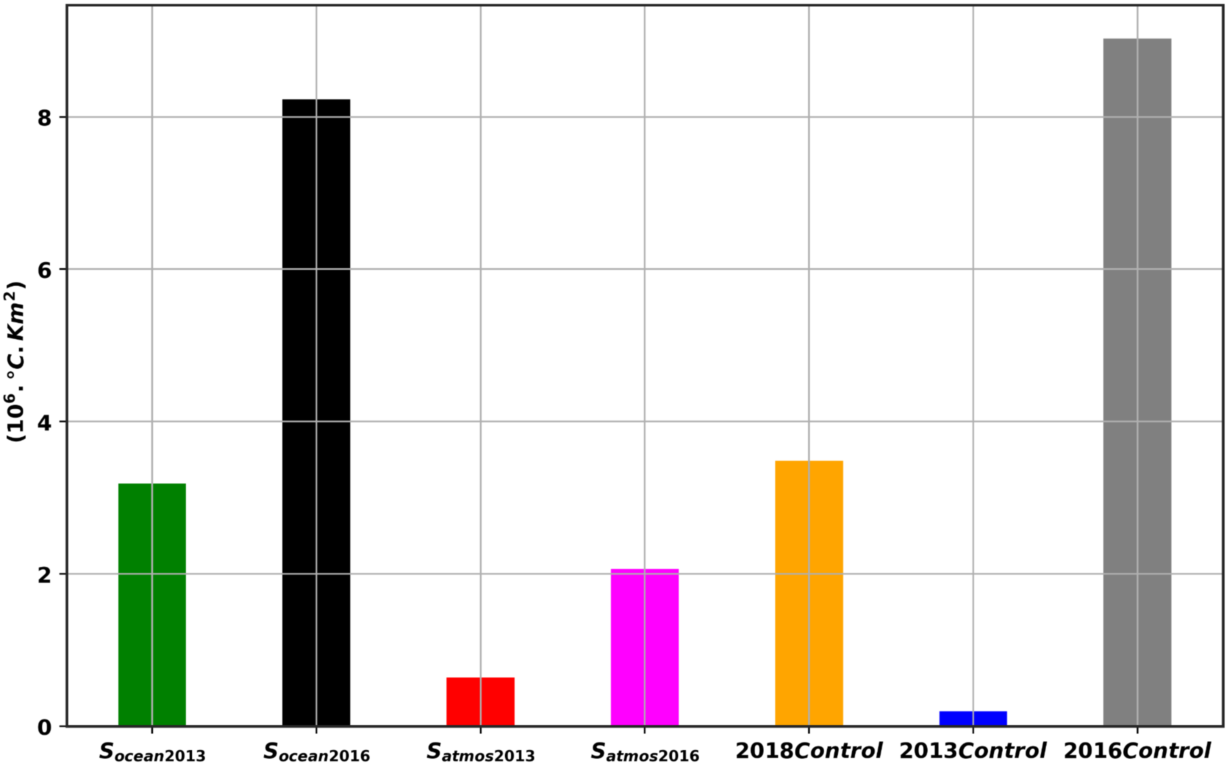

**Figure 12: A comparison of the MWP intensity index in all three experiments during the respective mature phase days in different years. In $S_{ocean2013}$, $S_{ocean2016}$, $S_{atmos2013}$, 2013 control experiment, and 2018 control experiment, the mature day was May 20. In the $S_{atmos2016}$ and 2016 control experiments, the mature day was May 4.**

### 2.8.2 Impact of Ocean Surface Flux in the Formation of the MWP

Once the ocean precondition was met, the atmospheric factors, including net surface heat flux, wind, and freshwater flux, played a leading role in shaping the spatial extent of MWP. The relative importance of net thermal flux, freshwater flux, and wind on mixing was examined here using potential turbulent kinetic energy ($P_{TKE}$). Contrary to wind stirring, the $P_{TKE}$ by haline and thermal buoyancy flux was of smaller magnitude in all the experiments, indicating that the wind was the driver for the mixing in SEAS in May (Fig. 13). The atmospheric conditions were similar in the 2018 control, $S_{ocean2013}$, and $S_{ocean2016}$ experiments (see Table 1 for experiment details). From 1st to 5th May, the average $P_{TKE}$ caused by wind stirring was more than 8 $W.m^{-2}$; however, in the SEAS, a small wind shadow zone was formed with a very low $P_{TKE}$ (Fig. 14a). Subsequently, the mixing reduced, and expansion of MWP SST was observed within this wind shadow zone in 2018 control, $S_{ocean2013}$, and $S_{ocean2016}$ experiments. A similar but much-widened wind shadow zone was developed in the SEAS from 17th to 20th May, resulting in the largest MWP expansion in 2018 control, $S_{ocean2013}$, and $S_{ocean2016}$ experiments. Once the southwesterly wind strengthened, the $P_{TKE}$ increased, and the ocean lost heat at the surface (Fig. 13a and 14a). In the 2013 control and $S_{atmos2013}$ experiments, atmospheric conditions were identical, and the ocean gained heat (Fig. S11b in the supplementary). The wind-induced $P_{TKE}$ was more in SEAS, and no such wind shadow zone was developed (Fig 14b). Subsequently, the MWP was absent in these two experiments. In the 2016 control and $S_{atmos2016}$ experiments, the wind shadow zone was expanded over a comparatively large area from the 1st to the 8th of May (Fig. 14c). Besides, the ocean received heat during this time in SEAS, making a favorable condition for the development of the strong MWP (Fig. 11c in supplementary).

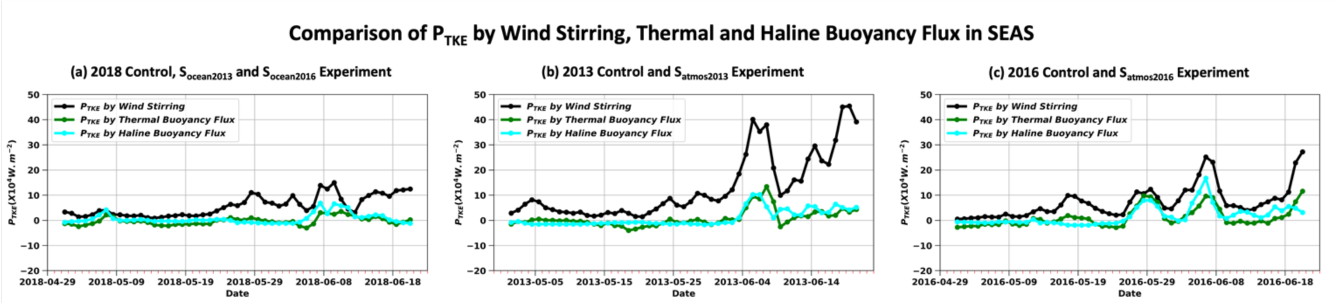

**Fig. 13 Comparision of PTKE by wind, thermal, and haline buoyancy flux averaged in the SEAS (72-76°E and 7-13°N) from May 1 to June 20. The values are shown here after multiplying $10^4$.**

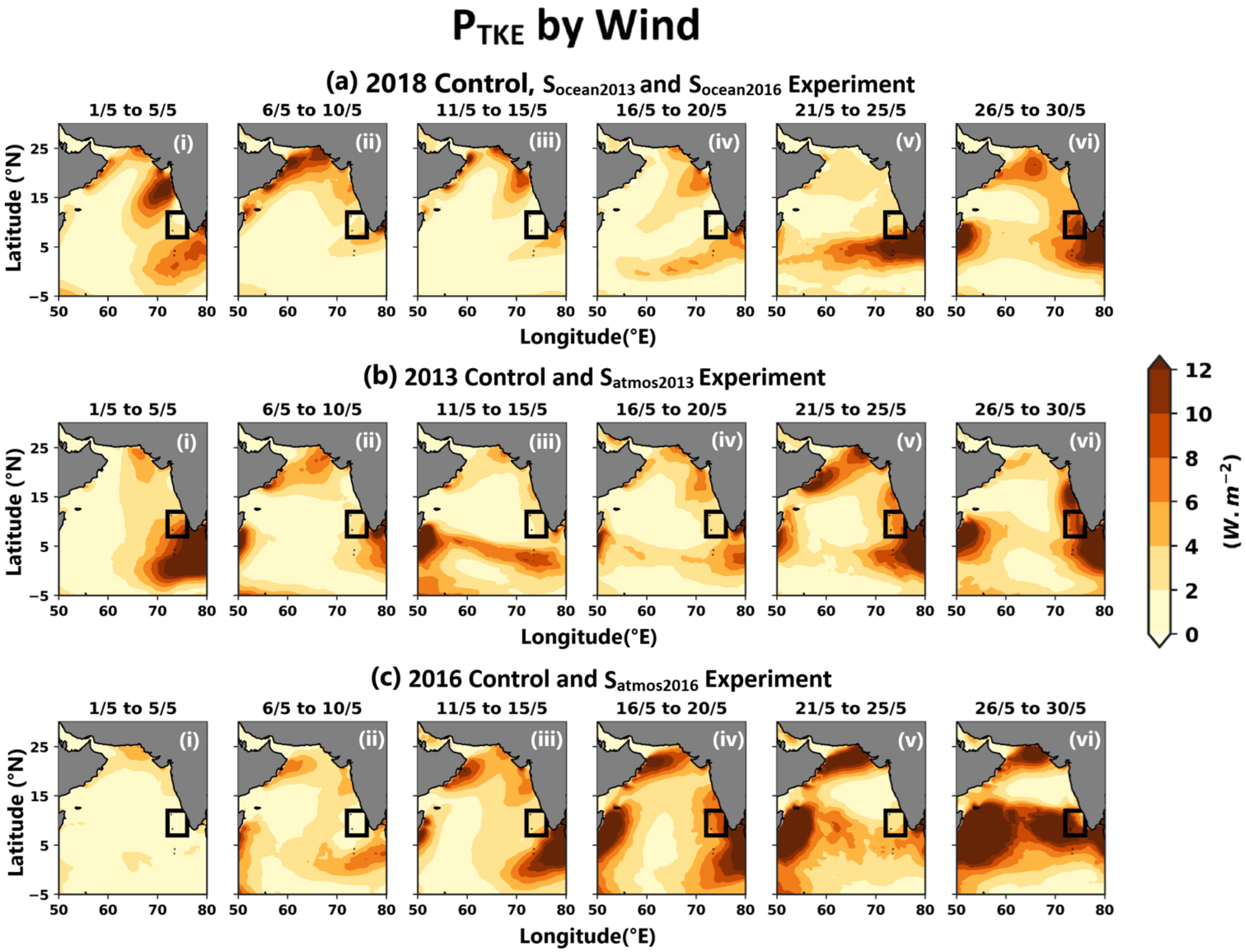

**Figure 14: 5-day average evolution of wind-induced production of turbulent kinetic energy ($P_{TKE}$) for all control and sensitivity experiments. The fill values are showing after multiplying $10^4$. Atmospheric forcings are identical for the 2018 control, $S_{ocean2013}$, and $S_{ocean2016}$ experiments. Likewise, the $P_{TKE}$ remains the same across all three experiments (a). Similarly, the $P_{TKE}$ owing to thermal buoyancy flux in the 2013 control experiment and $S_{ocean2013}$ (b) and the 2016 control experiment and $S_{ocean2016}$ (c) are identical. Table 1 shows details from the sensitivity experiments. The days associated with mean evolution are listed at the top of each subplot.**

## 3 Conclusion

A coupled atmosphere-ocean numerical model has been employed to investigate the formation and evolution of the MWP in the SEAS. The model is simulated for three independent years: 2013, 2016, and 2018. The simulated results can reproduce the MWP features and showed good agreement with satellite and buoy data (Fig. 2 to 5 and Fig. S2 to S5 in supplementary). The evolution of the atmospheric and ocean features near the SEAS from mature to dissipation day is well represented in the model. Four sensitivity experiments further elucidated the roles of oceanic and atmospheric conditions in the MWP formation. The changes in ocean initial conditions substantially impacted the magnitude of the MWP core temperature, resulting in 0.6°C higher in $S_{ocean2016}$ and 0.3°C lower in $S_{ocean2013}$ compared to the 2018 control experiment (Fig. S10d and S10e are compared with Fig. S10a in the supplementary), indicating the influence of the ocean initial condition in the MWP intensity. Analysis of the mixed-layer heat budget (Fig. 11) revealed that net surface heat flux is the primary driver of the MWP development, contributing significantly to the increase in mixed-layer temperature in the control and sensitivity experiments. It contributed more than 0.1°C per day to the increased temperature just before the MWP matured on the day of 2018. Vertical processes negatively affected temperature tendencies and could reach as high as -0.08°C/day. As the moisture-rich southwesterly wind strengthened in late May to early June, it caused cloudiness, blocking the incoming shortwave radiation and the loss of latent heat flux in the SEAS (Fig S6 and S8 in supplementary). Thus, the net surface heat flux, along with vertical processes, emerges as the primary driver behind the dissipation of the MWP (Fig. 11).

The atmospheric conditions remain the same in the 2018 control experiment, $S_{ocean2013}$, and $S_{ocean2016}$ experiments. Since the wind governs the MWP's advancement from mature to dissipation day by primarily controlling the net surface heat flux and the vertical processes, we have observed an identical contribution of the net surface heat flux and the vertical processes on the temperature tendency in these three experiments (Fig 11a,d, and e). The MWP did not emerge in 2013, and when we replaced the atmospheric (ocean) condition of the 2018 control experiment with the 2013 control experiment in the $S_{atmos2013}$ ($S_{ocean2013}$) sensitivity experiment, we saw an 82% reduction (8.5% reduction) in MWP intensity index when compared to the 2018 control experiment. This suggested that in the weak MWP year, although the ocean preconditions were met, the atmospheric forcing restricted the development of the MWP in SEAS. The MWP intensity index also revealed that shuffling of the atmospheric forcings and oceanic initial conditions of the strong MWP year to the year of the MWP whose intensity was identical to climatology ($S_{atmos2016}$ and $S_{ocean2016}$ experiment) resulted in a substantial decrease of 41% and increase of 136% in MWP intensity index (Fig. 12), which demonstrated that in the strong MWP year, the pre-April ocean condition played a considerable role in the development of the MWP in May which was further supported by the prevailing atmospheric conditions.

Later, $P_{TKE}$ was computed to study the mixing in the SEAS. The influence of wind-induced $P_{TKE}$ on mixing surpassed that of $P_{TKE}$ caused by thermal and haline buoyancy flux (Fig. 13). Further, a wind shadow zone with less $P_{TKE}$ was witnessed in SEAS. The MWP advanced within this zone (Fig. 14). However, this shadow zone was absent in experiments such as the 2013 control and $S_{atmos2013}$ experiments. The MWP did not develop in these two experiments, although the ocean preconditions were met, indicating that the wind shadow zone was a key factor in the MWP's advancement within the SEAS.

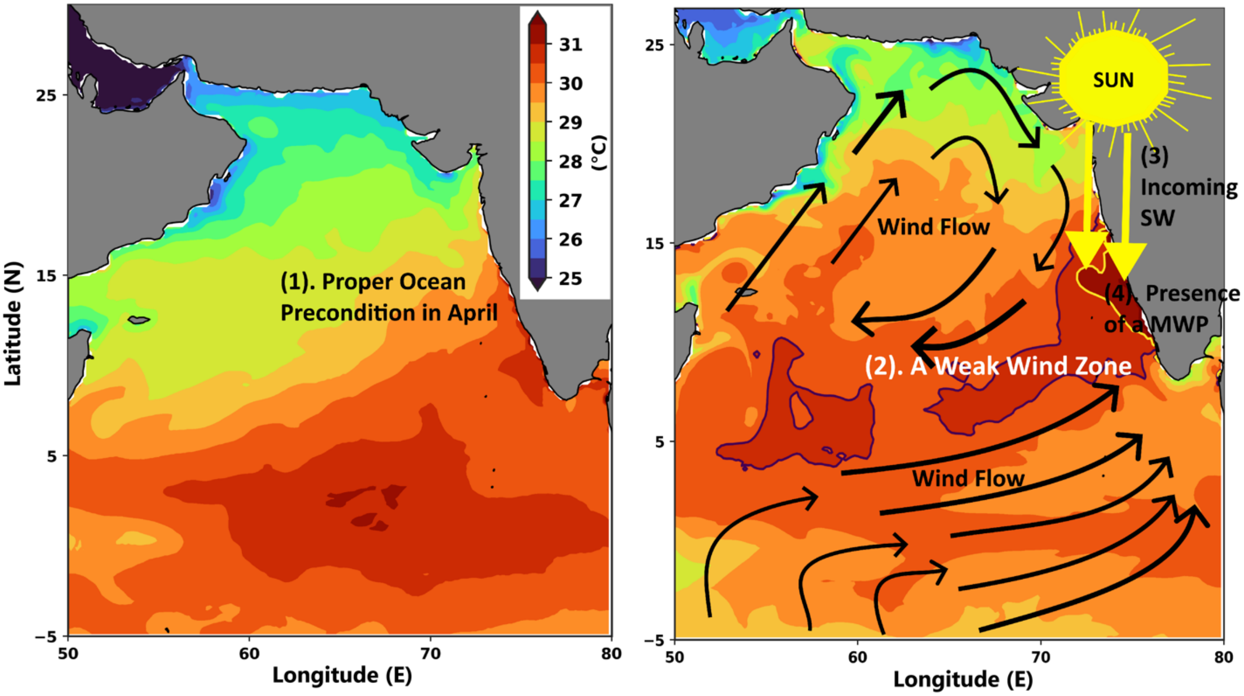

**Figure 15 Schematic of the atmospheric and oceanic conditions associated with the formation of the MWP. The numbering denotes the importance of that process in the formation of MWP. For instance, the ocean precondition (1) is the first requirement for MWP's genesis. Later, a weak wind zone (2) with less mixing traps the incoming shortwave radiation (3) in SEAS, which results in the formation of the MWP (4). Both the subplots have the same color bar levels. The black and yellow contours represent 30.5°C and 31°C, respectively.**

In conclusion, once the ocean conditions before April have laid the foundation ((1) in Fig. 15), the prevailing atmospheric conditions develop a weak wind zone in SEAS in May ((2) in Fig. 15), and the incoming shortwave radiation flux under the clear sky is trapped within this zone ((3) in Fig. 15). Subsequently, the MWP advances inside this area. Thus, a strong MWP can only occur in SEAS if all of these requirements are met (Fig. 15). After the MWP matures, the strong southwesterly wind in SEAS creates cloudiness and increases $P_{TKE}$, which blocks incoming shortwave radiation and causes the MWP to dissipate as the net surface heat flux decreases. The current study seeks to understand the impact of the ocean and atmosphere on the MWP during its mature phase and the factors that contribute to its dissipation. We concluded that atmospheric conditions such as wind influence the spatial variability of the MWP. Nonetheless, ocean pre-conditions before April have a substantial effect on MWP strength. Given the importance of ocean pre-conditioning in MWP genesis, it would be interesting to analyze the warming chronology of the southeastern Arabian Sea before the formation of a strong MWP, such as in 2016, which serves as the future scope of the current study. Besides, the wind shadow zone appears during a year with high MWP SST, and we hypothesize that this shadow zone and the resulting increase in MWP SST is linked with the onset of the Indian Summer Monsoon. However, further investigation is necessary, which is beyond the scope of the present study.

**Data Availability:**

SODA3.4.2 data is used to give initial and boundary conditions to the ocean part of the numerical model (Carton et al., 2018), whereas ERA5 data is used for the atmospheric boundary and initial condition (Hersbach et al., 2020). NOAA-AVHRR SST data is downloaded from https://www.ncei.noaa.gov/products/avhrr-pathfinder-sst (Saha et al., 2018). OSCAR current data is used to validate the model (Bonjean & Lagerloef, 2002). AD10 moored buoy data is available in the INCOIS data portal (https://incois.gov.in/portal/datainfo/mb.jsp). All the model output data used in this study are available upon request.

**Software Availability:**

Authors gratefully acknowledge USGS for making the COAWST numerical model available openly. In this study, python is used for the graphical plots. In addition, the Gibbs Seawater package (McDougall & Barker 2011) (https://www.teos-10.org/software.htm#1) is utilized to compute basic oceanic parameters. Further, wrf-python is used to handle the WRF output (Ladwig 2017). Software/programs related to the study may be available from the corresponding author upon request.

**Author Contributions:**

SPL ran the numerical models, analyzed the results, and wrote the first draft of the manuscript. KRP helped in analysis and manuscript editing. VP reviewed the manuscript and supervised the work. All the authors agreed to the final version of the manuscript.

**Competing Interests:**

The contact author has declared that none of the authors has any competing interests.

## Acknowledgments

This work is a part of SPL's doctoral thesis work. SPL is grateful to the Ministry of Education, Government of India, for awarding the Prime Minister's Research Fellowship (Ref: IITD/Admission/Ph.D./PMRF/2020-21/380299) for pursuing his doctoral research work at IIT-Delhi, India. The computational resources acquired through the high-performance computing (HPC) cluster at the IIT-Delhi are acknowledged. We thank the two anonymous reviewers for their insightful comments.

## References

Abram, N. J., Gagan, M. K., McCulloch, M. T., Chappell, J., & Hantoro, W. S. (2003). Coral reef death during the 1997 Indian Ocean Dipole linked to Indonesian wildfires. *Science*, *301*(5635). https://doi.org/10.1126/science.1083841

Akhil, V. P., Lengaigne, M., Krishnamohan, K. S., Keerthi, M. G., & Vialard, J. (2023). Southeastern Arabian Sea Salinity variability: mechanisms and influence on surface temperature. *Climate Dynamics*, *61*(7–8). https://doi.org/10.1007/s00382-023-06765-z

ARAKAWA, A., & LAMB, V. R. (1977). *Computational Design of the Basic Dynamical Processes of the UCLA General Circulation Model*. https://doi.org/10.1016/b978-0-12-460817-7.50009-4

Banzon, V., Smith, T. M., Mike Chin, T., Liu, C., & Hankins, W. (2016). A long-term record of blended satellite and in situ sea-surface temperature for climate monitoring, modeling and environmental studies. *Earth System Science Data*, *8*(1). https://doi.org/10.5194/essd-8-165-2016

Bonjean, F., & Lagerloef, G. S. E. (2002). Diagnostic model and analysis of the surface currents in the Tropical Pacific Ocean. *Journal of Physical Oceanography*, *32*(10). https://doi.org/10.1175/1520-0485(2002)032<2938:DMAAOT>2.0.CO;2

Boutin, J., Reul, N., Koehler, J., Martin, A., Catany, R., Guimbard, S., Rouffi, F., Vergely, J. L., Arias, M., Chakroun, M., Corato, G., Estella-Perez, V., Hasson, A., Josey, S., Khvorostyanov, D., Kolodziejczyk, N., Mignot, J., Olivier, L., Reverdin, G., … Mecklenburg, S. (2021). Satellite-Based Sea Surface Salinity Designed for Ocean and Climate Studies. *Journal of Geophysical Research: Oceans*, *126*(11). https://doi.org/10.1029/2021JC017676

Bruce, J. G., Johnson, D. R., & Kindle, J. C. (1994). Evidence for eddy formation in the eastern Arabian Sea during the northeast monsoon. *Journal of Geophysical Research*, *99*(C4). https://doi.org/10.1029/94JC00035

Bruce, J. G., Kindle, J. C., Kantha, L. H., Kerling, J. L., & Bailey, J. F. (1998). Recent observations and modeling in the Arabian Sea laccadive high region. *Journal of Geophysical Research: Oceans*, *103*(3334). https://doi.org/10.1029/97jc03219

Carniel, S., Benetazzo, A., Bonaldo, D., Falcieri, F. M., Miglietta, M. M., Ricchi, A., & Sclavo, M. (2016). Scratching beneath the surface while coupling atmosphere, ocean and waves: Analysis of a dense water formation event. *Ocean Modelling*, *101*. https://doi.org/10.1016/j.ocemod.2016.03.007

Carton, J. A., Chepurin, G. A., & Chen, L. (2018). SODA3: A new ocean climate reanalysis. *Journal of Climate*, *31*(17). https://doi.org/10.1175/jcli-d-18-0149.1

Chakraborty, T., Pattnaik, S., & Baisya, H. (2023). Investigating the precipitation features of monsoon deep depressions over the Bay of Bengal using high-resolution stand-alone and coupled simulations. *Quarterly Journal of the Royal Meteorological Society*, *149*(753). https://doi.org/10.1002/qj.4449

Chakraborty, T., Pattnaik, S., Baisya, H., & Vishwakarma, V. (2022). Investigation of Ocean Sub-Surface Processes in Tropical Cyclone Phailin Using a Coupled Modeling Framework: Sensitivity to Ocean Conditions. *Oceans*, *3*(3). https://doi.org/10.3390/oceans3030025

Dai, Q., Han, D., Rico-Ramirez, M. A., & Islam, T. (2013). The impact of raindrop drift in a three-dimensional wind field on a radar-gauge rainfall comparison. *International Journal of Remote Sensing*, *34*(21). https://doi.org/10.1080/01431161.2013.826838

Deepa, R., Seetaramayya, P., Nagar, S. G., & Gnanaseelan, C. (2007). On the plausible reasons for the formation of onset vortex in the presence of Arabian Sea mini warm pool. *Current Science*, *92*(6).

Doval, M. D., & Hansell, D. A. (2000). Organic carbon and apparent oxygen utilization in the western South Pacific and the central Indian Oceans. *Marine Chemistry*, *68*(3). https://doi.org/10.1016/S0304-4203(99)00081-X

Dudhia, J. (1989). Numerical study of convection observed during the Winter Monsoon Experiment using a mesoscale two-dimensional model. *Journal of the Atmospheric Sciences*, *46*(20). https://doi.org/10.1175/1520-0469(1989)046<3077:NSOCOD>2.0.CO;2

Durand, F., Shankar, D., de Boyer Montégut, C., Shenoi, S. S. C., Blanke, B., & Madec, G. (2007). Modeling the barrier-layer formation in the southeastern Arabian Sea. *Journal of Climate*, *20*(10). https://doi.org/10.1175/JCLI4112.1

Durand, F., Shetye, S. R., Vialard, J., Shankar, D., Shenoi, S. S. C., Ethe, C., & Madec, G. (2004). Impact of temperature inversions on SST evolution in the South-Eastern Arabian Sea during the pre-summer monsoon season. *Geophysical Research Letters*, *31*(1). https://doi.org/10.1029/2003GL018906

Foltz, G. R., & McPhaden, M. J. (2009). Impact of barrier layer thickness on SST in the central tropical North Atlantic. *Journal of Climate*, *22*(2). https://doi.org/10.1175/2008JCLI2308.1

Girishkumar, M. S., Joseph, J., Thangaprakash, V. P., Pottapinjara, V., & McPhaden, M. J. (2017). Mixed Layer Temperature Budget for the Northward Propagating Summer Monsoon Intraseasonal Oscillation (MISO) in the Central Bay of Bengal. *Journal of Geophysical Research: Oceans*, *122*(11). https://doi.org/10.1002/2017JC013073

Gopalakrishna, V. V., Johnson, Z., Salgaonkar, G., Nisha, K., Rajan, C. K., & Rao, R. R. (2005). Observed variability of sea surface salinity and thermal inversions in the Lakshadweep Sea during contrast monsoons. *Geophysical Research Letters*, *32*(18). https://doi.org/10.1029/2005GL023280

Haidvogel, D. B., Arango, H. G., Hedstrom, K., Beckmann, A., Malanotte-Rizzoli, P., & Shchepetkin, A. F. (2000). Model evaluation experiments in the North Atlantic Basin: Simulations in nonlinear terrain-following coordinates. *Dynamics of Atmospheres and Oceans*, *32*(3–4). https://doi.org/10.1016/S0377-0265(00)00049-X

Han, W., McCreary, J. P., & Kohler, K. E. (2001). Influence of precipitation minus evaporation and Bay of Bengal rivers on dynamics, thermodynamics, and mixed layer physics in the upper Indian Ocean. *Journal of Geophysical Research: Oceans*, *106*(C4). https://doi.org/10.1029/2000jc000403

Hareesh Kumar, P. V., Joshi, M., Sanilkumar, K. V., Rao, A. D., Anand, P., Anil Kumar, K., & Prasada Rao, C. V. K. (2009). Growth and decay of the Arabian Sea mini warm pool during May 2000: Observations and simulations. *Deep-Sea Research Part I: Oceanographic Research Papers*, *56*(4). https://doi.org/10.1016/j.dsr.2008.12.004

Hareesh Kumar, P. V., Sanilkumar, K. V., & Prasada Rao, C. V. K. (2007). Arabian sea mini warm pool and its influence on acoustic propagation. *Defence Science Journal*, *57*(1). https://doi.org/10.14429/dsj.57.1738

Hastenrath, S., & Greischar, L. L. (1989). Climatic atlas of the Indian Ocean. Part III: upper-ocean structure. *Climatic Atlas of the Indian Ocean. Part III: Upper-Ocean Structure*. https://doi.org/10.2307/635289

He, Q., Zhan, H., & Cai, S. (2020). Anticyclonic Eddies Enhance the Winter Barrier Layer and Surface Cooling in the Bay of Bengal. *Journal of Geophysical Research: Oceans*, *125*(10). https://doi.org/10.1029/2020JC016524

Hersbach, H., Bell, B., Berrisford, P., Hirahara, S., Horányi, A., Muñoz-Sabater, J., Nicolas, J., Peubey, C., Radu, R., Schepers, D., Simmons, A., Soci, C., Abdalla, S., Abellan, X., Balsamo, G., Bechtold, P., Biavati, G., Bidlot, J., Bonavita, M., … Thépaut, J. N. (2020). The ERA5 global reanalysis. *Quarterly Journal of the Royal Meteorological Society*, *146*(730). https://doi.org/10.1002/qj.3803

Hong, S. Y., Noh, Y., & Dudhia, J. (2006). A new vertical diffusion package with an explicit treatment of entrainment processes. *Monthly Weather Review*, *134*(9). https://doi.org/10.1175/MWR3199.1

Jacob, R., Larson, J., & Ong, E. (2005). M × N communication and parallel interpolation in community climate system model version 3 using the model coupling toolkit. *International Journal of High Performance Computing Applications*, *19*(3). https://doi.org/10.1177/1094342005056116

Kara, A. B., Rochford, P. A., & Hurlburt, H. E. (2000). An optimal definition for ocean mixed layer depth. *Journal of Geophysical Research: Oceans*, *105*(C7). https://doi.org/10.1029/2000jc900072

Kurian, J., & Vinayachandran, P. N. (2007). Mechanisms of formation of the Arabian Sea mini warm pool in a high-resolution Ocean General Circulation Model. *Journal of Geophysical Research: Oceans*, *112*(5). https://doi.org/10.1029/2006JC003631

Ladwig, W. (2017). *wrf-python (Version 1.3.2)*.

Large, W. G., McWilliams, J. C., & Doney, S. C. (1994). Oceanic vertical mixing: A review and a model with a nonlocal boundary layer parameterization. In *Reviews of Geophysics* (Vol. 32, Issue 4). https://doi.org/10.1029/94RG01872

Large, W. G., & Pond, S. (1981). Open ocean momentum flux measurements in moderate to strong winds. *J. PHYS. OCEANOGR.*, *11*(3, Mar. 1981). https://doi.org/10.1175/1520-0485(1981)011<0324:oomfmi>2.0.co;2

Li, N., Zhu, X., Wang, H., Zhang, S., & Wang, X. (2023). Intraseasonal and interannual variability of sea temperature in the Arabian Sea Warm Pool. *Ocean Science*, *19*(5), 1437–1451. https://doi.org/10.5194/os-19-1437-2023

Lim, K. S. S., & Hong, S. Y. (2010). Development of an effective double-moment cloud microphysics scheme with prognostic cloud condensation nuclei (CCN) for weather and climate models. *Monthly Weather Review*, *138*(5). https://doi.org/10.1175/2009MWR2968.1

Lukas, R., & Lindstrom, E. (1991). The mixed layer of the western equatorial Pacific Ocean. *Journal of Geophysical Research: Oceans*, *96*(S01). https://doi.org/10.1029/90jc01951

Masson, S., Luo, J. J., Madec, G., Vialard, J., Durand, F., Gualdi, S., Guilyardi, E., Behera, S., Delecluse, P., Navarra, A., & Yamagata, T. (2005). Impact of barrier layer on winter-spring variability of the southeastern Arabian Sea. *Geophysical Research Letters*, *32*(7). https://doi.org/10.1029/2004GL021980

Mathew, S., Natesan, U., Latha, G., & Venkatesan, R. (2018). Dynamics behind warming of the southeastern Arabian Sea and its interruption based on in situ measurements. *Ocean Dynamics*, *68*(4–5). https://doi.org/10.1007/s10236-018-1130-3

McDougall, Trevor J. ; Barker, P. M. (2011). Getting started with TEOS-10 and the Gibbs Seawater (GSW) Oceanographic Toolbox. *Scor/Iapso Wg127*.

Mlawer, E. J., Taubman, S. J., Brown, P. D., Iacono, M. J., & Clough, S. A. (1997). Radiative transfer for inhomogeneous atmospheres: RRTM, a validated correlated-k model for the longwave. *Journal of Geophysical Research Atmospheres*, *102*(14). https://doi.org/10.1029/97jd00237

Murty, V. S. N., Krishna, S. M., Nagaraju, A., Somayajulu, Y. K., Babu, V. R., Sengupta, D., Sindu, P. R., Ravichandran, M., & Rajesh, G. (2006). On the warm pool dynamics in the southeastern Arabian Sea during April-May 2005 based on the satellite remote sensing and ARGO float data. *Remote Sensing of the Marine Environment*, *6406*. https://doi.org/10.1117/12.694254

Neema, C. P., Hareeshkumar, P. V., & Babu, C. A. (2012). Characteristics of Arabian Sea mini warm pool and Indian summer monsoon. *Climate Dynamics*, *38*(9–10). https://doi.org/10.1007/s00382-011-1166-2

Nigam, T., Pant, V., & Prakash, K. R. (2018). Impact of Indian ocean dipole on the coastal upwelling features off the southwest coast of India. *Ocean Dynamics*, *68*(6). https://doi.org/10.1007/s10236-018-1152-x

Nyadjro, E. S., Subrahmanyam, B., Murty, V. S. N., & Shriver, J. F. (2012). The role of salinity on the dynamics of the Arabian Sea mini warm pool. *Journal of Geophysical Research: Oceans*, *117*(9). https://doi.org/10.1029/2012JC007978

Olabarrieta, M., Warner, J. C., Armstrong, B., Zambon, J. B., & He, R. (2012). Ocean-atmosphere dynamics during Hurricane Ida and Nor'Ida: An application of the coupled ocean-atmosphere-wave-sediment transport (COAWST) modeling system. *Ocean Modelling*, *43–44*. https://doi.org/10.1016/j.ocemod.2011.12.008

Olabarrieta, M., Warner, J. C., & Kumar, N. (2011). Wave-current interaction in Willapa Bay. *Journal of Geophysical Research: Oceans*, *116*(12). https://doi.org/10.1029/2011JC007387

Paul, N., Sukhatme, J., Gayen, B., & Sengupta, D. (2023). Eddy-Freshwater Interaction Using Regional Ocean Modeling System in the Bay of Bengal. *Journal of Geophysical Research: Oceans*, *128*(4). https://doi.org/10.1029/2022JC019439

PAULSON CA. (1970). MATHEMATICAL REPRESENTATION OF WIND SPEED ND TEMPERATURE PROFILES IN THE UNSTABLE ATMOSPHERIC SURFACE LAYER. *Journal of Applied Meteorology*, *9*(6).

Phillips, N. A. (1957). A COORDINATE SYSTEM HAVING SOME SPECIAL ADVANTAGES FOR NUMERICAL FORECASTING. *Journal of Meteorology*, *14*(2). https://doi.org/10.1175/1520-0469(1957)014<0184:acshss>2.0.co;2

Prakash, K. R., Nigam, T., & Pant, V. (2018). Estimation of oceanic subsurface mixing under a severe cyclonic storm using a coupled atmosphere-ocean-wave model. *Ocean Science*, *14*(2). https://doi.org/10.5194/os-14-259-2018

Prakash, K. R., & Pant, V. (2017). Upper oceanic response to tropical cyclone Phailin in the Bay of Bengal using a coupled atmosphere-ocean model. *Ocean Dynamics*, *67*(1). https://doi.org/10.1007/s10236-016-1020-5

Prakash, K. R., & Pant, V. (2020). On the wave-current interaction during the passage of a tropical cyclone in the Bay of Bengal. *Deep-Sea Research Part II: Topical Studies in Oceanography*, *172*. https://doi.org/10.1016/j.dsr2.2019.104658

PV Joseph. (1990). *Warm pool over the Indian Ocean and monsoon onset.*

Rao, R. R., & Sivakumar, R. (1999). On the possible mechanisms of the evolution of a mini-warm pool during the pre-summer monsoon season and the genesis of onset vortex in the South-Eastern Arabian Sea. *Quarterly Journal of the Royal Meteorological Society*, *125*(555). https://doi.org/10.1002/qj.49712555503

Rao, S. A., Gopalakrishna, V. V., Shetye, S. R., & Yamagata, T. (2002). Why were cool SST anomalies absent in the Bay of Bengal during the 1997 Indian Ocean Dipole event? *Geophysical Research Letters*, *29*(11). https://doi.org/10.1029/2001GL014645

Ricchi, A., Miglietta, M. M., Falco, P. P., Benetazzo, A., Bonaldo, D., Bergamasco, A., Sclavo, M., & Carniel, S. (2016). On the use of a coupled ocean-atmosphere-wave model during an extreme cold air outbreak over the Adriatic Sea. *Atmospheric Research*, *172–173*. https://doi.org/10.1016/j.atmosres.2015.12.023

Saha, K., Zhao, X., Zhang, H., Casey, K. S., Zhang, D., Baker-Yeboah, Sheekela., Kilpatrick, K. A., Evans, R. H., Ryan, T., & Relph, J. M. (2018). *AVHRR Pathfinder version 5.3 level 3 collated (L3C) global 4km sea surface temperature for 1981-Present.* NOAA National Centers for Environmental Information. Dataset.

Sandeep, K. K., Pant, V., Girishkumar, M. S., & Rao, A. D. (2018). Impact of riverine freshwater forcing on the sea surface salinity simulations in the Indian Ocean. *Journal of Marine Systems*, *185*. https://doi.org/10.1016/j.jmarsys.2018.05.002

Sanil Kumar, V., & Anjali Nair, M. (2015). Inter-annual variations in wave spectral characteristics at a location off the central west coast of India. *Annales Geophysicae*, *33*(2). https://doi.org/10.5194/angeo-33-159-2015

Sarma, V. V. S. S. (2006). The influence of Indian Ocean Dipole (IOD) on biogeochemistry of carbon in the Arabian Sea during 1997-1998. *Journal of Earth System Science*, *115*(4). https://doi.org/10.1007/BF02702872

Schott, F. A., & McCreary, J. P. (2001). The monsoon circulation of the Indian Ocean. In *Progress in Oceanography* (Vol. 51, Issue 1). https://doi.org/10.1016/S0079-6611(01)00083-0

Schott, F. A., Xie, S. P., & McCreary, J. P. (2009). Indian ocean circulation and climate variability. In *Reviews of Geophysics* (Vol. 47, Issue 1). https://doi.org/10.1029/2007RG000245

Seelanki, V., Nigam, T., & Pant, V. (2021). Upper-ocean physical and biological features associated with Hudhud cyclone: A bio-physical modelling study. *Journal of Marine Systems*, *215*. https://doi.org/10.1016/j.jmarsys.2020.103499

Seetaramayya, P., & Master, A. (1984). Observed air-sea interface conditions and a monsoon depression during MONEX-79. *Archives for Meteorology, Geophysics, and Bioclimatology Series A*, *33*(1). https://doi.org/10.1007/BF02265431

Shankar, D., Remya, R., Vinayachandran, P. N., Chatterjee, A., & Behera, A. (2016). Inhibition of mixed-layer deepening during winter in the northeastern Arabian Sea by the West India Coastal Current. *Climate Dynamics*, *47*(3–4). https://doi.org/10.1007/s00382-015-2888-3

Shankar, D., & Shetye, S. R. (1997). On the dynamics of the Lakshadweep high and low in the southeastern Arabian Sea. *Journal of Geophysical Research: Oceans*, *102*(C6). https://doi.org/10.1029/97JC00465

Shankar, D., Vinayachandran, P. N., & Unnikrishnan, A. S. (2002). The monsoon currents in the north Indian Ocean. In *Progress in Oceanography* (Vol. 52, Issue 1). https://doi.org/10.1016/S0079-6611(02)00024-1

Shee, A., Sil, S., Gangopadhyay, A., Gawarkiewicz, G., & Ravichandran, M. (2019). Seasonal Evolution of Oceanic Upper Layer Processes in the Northern Bay of Bengal Following a Single Argo Float. *Geophysical Research Letters*, *46*(10). https://doi.org/10.1029/2019GL082078

Shenoi, S. S. C., Shankar, D., & Shetye, S. R. (1999). On the sea surface temperature high in the Lakshadweep Sea before the onset of the southwest monsoon. *Journal of Geophysical Research: Oceans*, *104*(C7). https://doi.org/10.1029/1998jc900080

Skamarock, W. C., & Klemp, J. B. (2008). A time-split nonhydrostatic atmospheric model for weather research and forecasting applications. *Journal of Computational Physics*, *227*(7). https://doi.org/10.1016/j.jcp.2007.01.037

Skamarock WC, et al. (2008). A description of the advanced research WRF version 3, NCAR Tech. Note, NCAR/TN-468+STR. *Natl. Cent. for Atmos. Res. Boulder, Colorado*, *June*.

Song, Y., & Haidvogel, D. (1994). A semi-implicit ocean circulation model using a generalized topography-following coordinate system. *Journal of Computational Physics*, *115*(1). https://doi.org/10.1006/jcph.1994.1189

Sprintall, J., & Tomczak, M. (1992). Evidence of the barrier layer in the surface layer of the tropics. *Journal of Geophysical Research: Oceans*, *97*(C5). https://doi.org/10.1029/92jc00407

Stevenson, J. W., & Niiler, P. P. (1983). Upper Ocean Heat Budget During the Hawaii-to-Tahiti Shuttle Experiment. *Journal of Physical Oceanography*, *13*(10). https://doi.org/10.1175/1520-0485(1983)013<1894:uohbdt>2.0.co;2

Tewari, M., Chen, F., Wang, W., Dudhia, J., LeMone, M. A., Mitchell, K., Ek, M., Gayno, G., Wegiel, J., & Cuenca, R. H. (2004). Implementation and verification of the unified noah land surface model in the WRF model. *Bulletin of the American Meteorological Society*.

Umlauf, L., & Burchard, H. (2003). A generic length-scale equation for geophysical turbulence models. *Journal of Marine Research*, *61*(2). https://doi.org/10.1357/002224003322005087

Vialard, J., Foltz, G. R., McPhaden, M. J., Duvel, J. P., & de Boyer Montégut, C. (2008). Strong Indian Ocean sea surface temperature signals associated with the Madden-Julian Oscillation in late 2007 and early 2008. *Geophysical Research Letters*, *35*(19). https://doi.org/10.1029/2008GL035238

Warner, J. C., Armstrong, B., He, R., & Zambon, J. B. (2010). Development of a Coupled Ocean-Atmosphere-Wave-Sediment Transport (COAWST) Modeling System. *Ocean Modelling*, *35*(3). https://doi.org/10.1016/j.ocemod.2010.07.010

Zambon, J. B., He, R., & Warner, J. C. (2014). Investigation of hurricane Ivan using the coupled ocean–atmosphere–wave–sediment transport (COAWST) model. *Ocean Dynamics*, *64*(11). https://doi.org/10.1007/s10236-014-0777-7

Zhang, C., & Wang, Y. (2017). Projected future changes of tropical cyclone activity over the Western North and South Pacific in a 20-km-Mesh regional climate model. *Journal of Climate*, *30*(15). https://doi.org/10.1175/JCLI-D-16-0597.1